

A shallow neural network trained to detect collisions recovers features of visual loom-selective neurons

Firstname Middlename Surname^{1*}, Firstname Middlename Familyname^{1,2†§},
Firstname Initials Surname^{2‡¶}, Firstname Surname^{2*}

*For correspondence:

damon.clark@yale.edu (DAC);
john.lafferty@yale.edu (JDL)

[†]These authors contributed equally
to this work

[‡]These authors also contributed
equally to this work

Present address: [§]Department,
Institute, Country; [¶]Department,
Institute, Country

¹Institution 1; ²Institution 2

Abstract Animals have evolved sophisticated visual circuits to detect looming objects. Studies of the visual system of *Drosophila* have revealed that looming stimuli are selectively encoded by a suite of neurons, including LPLC2 neurons. In LPLC2 neurons, the dendrites are arranged in a distinctive anatomical structure and receive excitatory and inhibitory inputs that cause them to respond selectively to the radial expansion of the edges of a looming object. Our study aims to understand how the computations in LPLC2 neurons are related to the inference problem that the neuron appears to be solving: whether an object is looming towards the fly. To do this, we trained anatomically-constrained shallow neural networks to detect whether or not a visual signal is an object on a collision course. We used these trained inference models to ask how known properties of the biological neural circuits relate to the features of the artificial neural network trained on synthetic visual stimuli. We trained a single unit of our model on a set of diverse artificial visual stimuli to detect whether moving objects were on a collision course with the detector location. Surprisingly, the model arrived at two distinct solutions to this detection problem: one with dendritic weighting that mirrored LPLC2 and the other selective for inward-directed motion. We analyzed how each of these two solutions work to detect looming events. When we increased the number of units in the population, the performance of the model improved, and weighting similar to LPLC2 became more favored. When many units tiled visual space, the trained models also exhibited many of the response properties measured in LPLC2. Our findings suggest that LPLC2 can be understood as solving an inference problem, and that signals from the entire population of LPLC2 neurons are critical for understanding how LPLC2 reliably encodes looming stimuli.

Introduction

For animals living in dynamic visual environments, it is important to detect the approach of predators or other dangerous objects. Many species, from insects to humans, rely on a range of visual cues to identify approaching, or looming, objects (Regan and Beverley, 1978; Sun and Frost, 1998; Gabiani et al., 1999; Card and Dickinson, 2008; Münch et al., 2009; Temizer et al., 2015). Among other cues, looming objects create characteristic visual flow fields. When an object is on a ballistic collision course with an animal, its edges will appear to the observer to expand radially outward, gradually occupying a larger and larger portion of the visual field. An object heading towards the animal, but which will not collide with it, also expands to occupy a larger and larger portion of the visual field, but its edges do not expand radially outwards. Instead, its edges expand outwards but its center also moves so that opposite edges are not moving in opposite directions. A collision detector must distinguish between these two cases, while also avoiding predicting collisions in response to

41 myriad other visual flow fields created by the animal's own motion. Thus, loom detection can be
 42 framed as a visual inference problem.

43 Many sighted animals solve this inference problem and detect looming objects with high
 44 precision, thanks to the robust looming-selective neural circuits evolved over hundreds of millions
 45 of years. Humans respond to unexpected approaching objects with defensive movements (*King*
 46 *et al., 1992*). Even when people have damage in cortical area V1, the sensitivity to looming stimuli
 47 remains intact, routed through sub-cortical pathways (*Hervais-Adelman et al., 2015*). Similar to
 48 adults, weeks-old infants respond selectively to looming signals versus non-looming ones (*Ball*
 49 *and Tronick, 1971*). The defensive and fear responses to approaching objects are also prevalent
 50 in other mammals, such as cats (*Liu et al., 2011*) and mice (*Yilmaz and Meister, 2013; Shang et al.,*
 51 *2015; Salay et al., 2018*). Specific neural pathways both in retina (*Yilmaz and Meister, 2013*) and
 52 midline thalamus (*Salay et al., 2018*) have been proposed to mediate the escaping or freezing
 53 behaviors of mice. Moreover, in both the cat and mouse, various cell types have been identified
 54 in the superior colliculus that encode different information about the looming events, such as
 55 the angular size and expanding speed of the edges (*Liu et al., 2011; Shang et al., 2015*). Similar
 56 differentiations of the roles of distinct cell types in looming detections have been also found in the
 57 tectum of pigeon (*Wu et al., 2005*) and zebrafish (*Temizer et al., 2015; Dunn et al., 2016*). In zebra
 58 fish's brainstem, bilateral Mauthner cells trigger evasive turns during presentations of looming
 59 visual signals (*Bhattacharyya et al., 2017*).

60 In invertebrates, detailed anatomical, neurophysiological, behavioral and modeling studies
 61 have investigated loom detection, especially in locusts and flies (*Oliva and Tomsic, 2014; Sato*
62 and Yamawaki, 2014; Santer et al., 2005; Gabbiani et al., 1999; Rind and Bramwell, 1996; Card
63 and Dickinson, 2008; De Vries and Clandinin, 2012; Muijres et al., 2014; Klapoetke et al., 2017;
64 Von Reyn et al., 2017; Ache et al., 2019). An influential mathematical model of loom detection was
 65 derived by studying the responses of the giant descending neurons of locusts, which established a
 66 relationship between the timing of the neurons' peak responses and an angular size threshold for
 67 the looming object (*Gabbiani et al., 1999*). Similar models have been applied to analyze looming
 68 signals in other animals, including in flies (*Von Reyn et al., 2017; Ache et al., 2019*). In flies, where
 69 genetic tools make it possible to precisely dissect neural circuits, various neuron types have been
 70 revealed to be sensitive to looming signals (*Von Reyn et al., 2017; Ache et al., 2019; Morimoto et al.,*
71 2020).

72 The loom-sensitive neuron PLC2 (lobula plate/lobula columnar, type II) (*Wu et al., 2016*) has been
 73 studied in detail (*Klapoetke et al., 2017*). These neurons tile visual space. They send their axons to
 74 a descending neuron called the giant fiber and contributes to the fly's jumping or takeoff behaviors
 75 triggered by expanding discs (*Card and Dickinson, 2008; Ache et al., 2019*). Each LPLC2 neuron
 76 has four dendritic branches that receive inputs from the four layers of the lobula plate (LP) (Fig.
 77 1A) (*Maisak et al., 2013; Klapoetke et al., 2017*). The retinotopic LP layers host the axon terminals
 78 of motion detection neurons, and each layer uniquely receives motion information in one of the
 79 four cardinal directions (*Maisak et al., 2013*). Thus, each of the four LPLC2 dendrites selectively
 80 integrates motion information in one of the four cardinal directions. Moreover, the physical
 81 extensions of the LPLC2 dendrites align with the preferred motion directions in the corresponding
 82 LP layers (Fig. 1B) (*Klapoetke et al., 2017*). These dendrites form an outward radial structure, which
 83 matches the moving edges of a looming object that expands in the visual field (Fig. 1C). Other
 84 common stimuli such as the whole-field motion generated by self-turning only match part of the
 85 radial structure (one or two branches depending on the axis of the turning), and strong inhibition
 86 for inward-directed motion suppresses responses to such stimuli (*Klapoetke et al., 2017*). Thus, the
 87 structure of the LPLC2 dendrites favors responses to objects with edges moving radially outwards,
 88 that is, objects that approach from the center of its receptive field.

89 Although the dendritic structure of the LPLC2 neuron (and many other features of the fly visual
 90 system) are genetically coded and not thought to be shaped by the fly's visual experience, they
 91 did arise through evolution, where they won the natural selection battle against other possible

92 structures. We wanted to investigate whether we could understand the loom computation in LPLC2
 93 as the optimized solution to an inference problem. Can the structure of LPLC2 inputs be explained
 94 by optimized inference of collision courses? Moreover, since there are more than 200 LPLC2 neurons
 95 tiling a fly's visual system, and their receptive fields tile the visual space with substantial overlap
 96 (*Klapoetke et al., 2017; Ache et al., 2019*), can we understand how this population of signals relates
 97 to the computational structures of individual LPLC2 neurons.

98 To answer these questions, we built a simple anatomically-constrained loom detector, which
 99 receives positive and negative inputs from motion signals in the four cardinal directions. We
 100 trained the model on artificial stimuli, where its task was to selectively respond to visual objects
 101 on a collision course with the detector. Surprisingly, this binary classification task leads to two
 102 distinct types of solutions, with one resembling the LPLC2 neurons but the other having an opposite
 103 configuration. We analyzed how each of these solutions detected looming events and where they
 104 show distinct individual and population behaviors. Interestingly, when we increased the number of
 105 units tiling visual space, the solutions that resemble the LPLC2 neurons perform better and become
 106 more favored. We tested the trained inference models on visual stimuli not in their training data
 107 and show that they reproduce the response curves of real LPLC2 neurons (*Klapoetke et al., 2017*).
 108 Our results show that XXXX.

109 Results

110 A set of artificial visual stimuli

111 Our goal is to compare models trained to perform loom-detection with the biological computations
 112 in LPLC2. To do that, we must create a set of stimuli that can act as training data for the inference
 113 task. For this, we considered the following four types of motion stimuli: loom-and-hit (hit for short),
 114 loom-but-miss (miss for short), retreat, and rotation (Fig. 2). The loom-and-hit stimulus consists
 115 of a sphere that moves ballistically towards the origin on a collision course. The loom-but-miss
 116 stimulus is a sphere that moves ballistically towards the origin but misses it. The retreat stimulus is
 117 a sphere moving ballistically away from the origin. And the rotation stimulus consists of objects
 118 rotating about an axis. All stimuli were designed to be isotropic: the first three stimuli could have
 119 any orientation in space, while the rotation could be about any axis. All trajectories were simulated
 120 in the frame of reference of the model fly at the origin, so that distances of objects are measured
 121 with respect to the fly. For simplicity, the fly is assumed to be a point particle with no volume
 122 (Red dots in Fig. 2) and the apexes of the cones in Fig. 3). In the hits, misses, and retreats, the
 123 spherical object has unit radius, and for the case of rotation, there were 100 objects with various
 124 radii scattered isotropically about the fly (Fig. 3).

125 An anatomically-constrained mathematical model for inferring loom

126 We built a simple, anatomically-constrained neural network (Fig. 4) to infer the chance that a moving
 127 object hits the fly. The features of this network were designed to mirror some anatomy of the fly's
 128 LPLC2 neurons 1.

129 Model units receive inputs from a 60 degree diameter cone of visual space, represented by white
 130 cones and grey circles in Fig. 3), mirroring the receptive field size measured for LPLC2 (*Klapoetke*
 131 *et al., 2017*). The four stimulus sets were projected into this receptive field size for training and
 132 evaluating the model.

133 The inputs to the model were not intensity, but rather local directional signals, computed in the
 134 four cardinal directions at each point of visual space: downward, upward, rightward, and leftward
 135 (Fig. 3). These four cardinal directions of motion signals represent the motion signals from T4
 136 and T5 neurons in the four layers of the lobula plate (*Maisak et al., 2013*). They were computed as
 137 the non-negative components of a simple Hassenstein-Reichardt correlator model (*Hassenstein*
 138 *and Reichardt, 1956*) in both horizontal and vertical directions, which acted on the intensity of the
 139 projected stimuli (see Methods). The motion signals were computed with a spacing of 5 degrees,

140 roughly matching the spacing the ommatidia and processing columns in the fly eye (*Stavenga, 2003*). [cite]

141 Each model unit can weight the motion signals from the four layers using linear spatial filters.
 142 There are two sets of non-negative filters, the excitatory ones and the inhibitory ones (red and
 143 blue in Fig. 4A), respectively). Each set has four branches, integrating motion signals from the four
 144 cardinal directions, respectively. These spatial filters represent excitatory inputs to LPLC2 directly
 145 from T4 and T5 and inhibitory ones mediated by local interneurons (*Klapoetke et al., 2017; Mauss*
 146 *et al., 2015*). All eight filters act on the 60 degree diameter receptive field of an LPLC2 unit. A
 147 90-degree rotation symmetry is imposed among the filters, so that filters on each layer are identical.
 148 Moreover, each filter is symmetric about the axis of motion (see Methods). No further assumptions
 149 are made about the specific structures of the filters.
 150

151 There is one fundamental difference between the excitatory and inhibitory branches: the
 152 integrated signals from each excitatory branch are sent directly to the downstream computations,
 153 while the integrated signals from each inhibitory branch are rectified before being sent downstream.
 154 This difference reflects the anatomical constraints of the inputs to a real LPLC2 neuron: the
 155 excitatory inputs come from the dendrites of the same LPLC2 neuron while the inhibitory inputs are
 156 from individual interneurons (LPI) between LP layers (*Mauss et al., 2015; Klapoetke et al., 2017*).
 157 The outputs of the eight branches are then summed and rectified to generate the responses of a
 158 single model unit given the optical stimuli (Fig. 4A).

159 A population of LPLC2 neurons converge onto to the giant fiber (Fig. 1D). Thus, in our model,
 160 there are M replicates of each model unit, and the unit orientations are spread evenly over the 4π
 161 steradians of the unit sphere (see Methods). In this way, the receptive fields of the M units roughly
 162 tile the whole angular space with or without overlap, depending on the value of M . The sum of the
 163 responses of the M mdoel units is fed into a sigmoid function to generate the probability of hit for
 164 a given trajectory.

165 **Two distinct solutions to the loom-inference problem**

166 In this section, we will show how the binary classification task on the artificial stimuli shapes the
 167 structures of the excitatory and inhibitory filters, and moreover, what effects the number of LPLC2
 168 units M will have on the results.

169 We started from the simplest model where there is only one LPLC2 unit, i.e., $M = 1$, and the
 170 task of the model is to distinguish the motion signals that are generated by hitting objects from
 171 the motions signals generated by other types of motions (Fig. 2), Fig. 3). The models were trained
 172 from 200 different random initializations, and the converged solutions fell into three categories,
 173 represented by three colors: black, magenta, and green (Fig. 5A, B). The black solutions are
 174 unstructured, and will be ignored. The other two structured solutions are the interesting ones,
 175 and surprisingly, they have exactly the opposite structures. Based on the configurations of the
 176 excitatory filters (METHOD), the two types of solutions are called outward filters (magenta) and
 177 inward filters (green), respectively (Fig. 5C) and Fig. 1A). The outward excitatory filters resemble
 178 the dendritic structures of the real LPLC2 neurons observed in experiments, where for example,
 179 the rightward motion sensitive branch (LP2) occupies mainly the right side of the receptive field. In
 180 addition, our model indicates that in the outward case, the rightward motion-sensitive inhibitory
 181 filter mainly occupies the left side of the receptive field. This is consistent with the properties of
 182 the lobula plate intrinsic (LPI) interneurons that project inhibitory signals from one LP layer to the
 183 adjacent one with the opposite directional sensitivity (*Mauss et al., 2015; Klapoetke et al., 2017*).

184 The unexpected inward solutions are exactly the opposite of the outward ones, with the right-
 185 ward sensitive excitatory filter occupies the left side of the receptive field, and the inhibitory filter
 186 the right side. This is a strange structure, and it seems that it cannot detect looming signals at all.
 187 In fact, the activity of this inward unit will be suppressed if the hitting objects are looming from
 188 the center of the receptive field. However, in this single-unit model, the inward solutions actually
 189 performs better than the outward ones in the task of distinguishing the hit cases from the non-hit

190 cases (Fig. 5D) and Fig. 1B). This puzzling result might come from the fact that the single-unit model
 191 can only see a portion of stimuli in the hit, miss and retreat cases, since their distributions are
 192 spherically symmetric, and this makes the training problematic. Thus, we want to know whether
 193 the two opposite solutions still exist as we include more LPLC2 units in the model.

194 When the number of LPLC2 units M increases, they can cover more angular space, and if M
 195 is large enough, the receptive field of the units start to overlap with each other (Fig. 6A). In the
 196 brain of a real fly, there are over 200 LPLC2 neurons, and this actually corresponds to a very dense
 197 distribution of the units, as shown by the third row in Fig. 6A where $M = 256$. When M is large, all
 198 signals are detected and in fact, any signal can be detected simultaneously by many LPLC2 units
 199 from different angles. Interestingly, the two oppositely structured solutions persist, regardless of
 200 the value of M , as shown in Fig. 6, Fig. 1), Fig. 2), Fig. 3). We noticed that in outward solutions,
 201 there are structures on the right side of the inhibitory filters that looks like the structures of the
 202 corresponding excitatory filters. This indicates that there might be some redundancy in our model,
 203 and sometimes, this structure does not exist for other outward solutions (Fig. 2, Fig. 3).

204 **The outward and inward filters are selective to hit signals with different eccentricities**

205 To understand the differences between the two types of solutions and why the inward ones can
 206 even exist, let's take a look at how they respond to hit stimuli from different incoming angles θ
 207 (Fig. 7A). First, when there are no signals, the baseline activities of outward units are zero, but the
 208 baseline activities of inward units are above zero (grey dashed lines in Fig. 7B, C). This is because
 209 the trained intercepts are negative in the outward case, but positive in the inward case (METHOD).
 210 Second, as shown in Fig. 7B,C), the outward filters respond strongly to the stimuli near the center of
 211 the receptive field, but do not respond to stimuli with large angles (bigger than 30°). However, for
 212 the inward filters, they respond negatively to the stimuli coming from the center but positively to
 213 stimuli coming from the periphery of the receptive field with angles between 30° and 90° (Fig. 7B,
 214 C). This explains why the inward units are proper looming detectors. In fact, if we assume that hit
 215 signals are isotropic as shown in Fig. 2A), then we can show that the number of stimuli within the
 216 angles 30° and 90° is much larger than the number of stimuli with the angles below 30° (Fig. 7D).
 217 Thus, the inward solutions can detect much more possible hit cases than the outward ones. In Fig.
 218 7E), we show heatmaps of the responses of the models in terms of distance to the eye and the
 219 incoming angles. For the hit cases, the response patterns are consistent with Fig. 7C). As expected,
 220 the inward solutions respond to the retreating signals with angles near 180°, since the motions of
 221 edges coincide with their filter structures.

223 **The outward solutions have sparse codings while the inward ones have dense codings**

224 We have seen that the individual units of the two models are very different from each other in their
 225 filter structures and response patterns to hit or other stimuli. In this section, we turn to population
 226 activities, and show that these differences in the individual level lead to distinct population codes
 227 when a group of LPLC2 units work together to predict the probability of hit.

228 As shown in Fig. 8A), the outward and inward units exhibit different population response
 229 patterns for a given hit stimulus. Active outward units usually respond more strongly than inward
 230 ones, but more inward units will be activated than outward ones. In fact, this is consistent with
 231 what has been found in the last section that for a given LPLC2 unit, there are more hitting incidents
 232 from the periphery of its receptive field than from the center. At each time point, the sum of the
 233 activities of the LPLC2 units is used to infer the probability of hit, and thus both outward and inward
 234 models give similar probabilities of hit for this stimulus as shown in the last row of the Fig. 8A).

235 In Fig. 8B), the inferred probabilities of hit for different types of stimuli are summarized for both
 236 the outward and inward solutions. It can be seen that both types of models can give reasonable
 237 inferences. Some of the misses are very close to the eye, and thus, they look like hits. We plotted

239 the probability of hit against the minimum distance to the eye for the misses (Fig. 8C), and it can be
 240 seen clearly that near misses have higher probabilities of hit than far misses.

241 **Large populations of units improve performance and favor outward filters over
 242 inward ones**

243 Since more LPLC2 units will cover larger spacial area of the visual field, and they also will provide
 244 more information about the incoming signals, the models perform better when the population
 245 of LPLC2 cells M increases (Fig. 9A). In fact, when M is above 32, both the ROC-AUC and PR-AUC
 246 scores are almost 1 (METHOD), which indicates that the predictive power of the model is beyond
 247 the difficulties of the binary classification task on the four types of synthetic data.

248 We have shown that the counter-intuitive inward filters are actually reasonable solutions to
 249 the looming detection task. However, it is still unclear why the biological LPLC2 neurons have
 250 these outward structures rather than inward ones. To answer this question, we plotted the ratio of
 251 the number of outward filters and the number of inward filters that arise out of the 200 random
 252 initializations against the population size M , and interestingly, it shows that there are more outward
 253 filters when the models have more LPLC2 units (Fig. 9B). For the model with 256 LPLC2 cells, the
 254 chance that an outward filter appears from the training is almost 4 times larger than that of an
 255 inward filter. This result suggests that during evolution, it is more likely for the fly's visual system
 256 to adopt the outward solution rather than the inward one, since for a fly there are more than 200
 257 LPLC2 neurons.

258 Although both outward and inward models with large M have similar ROC-AUC and PR-AUC
 259 scores, the cross entropy loss functions show that outward filters have lower losses than inward
 260 ones when the population of LPLC2 units is large (Fig. 9C). This is consistent with the fact that the
 261 training ended up with more outward models than inward ones for larger LPLC2 population size M .

262 **Replications of biological data**

263 As has been discussed, the outward models have similar structures to biological LPLC2 neurons, and
 264 these structures are obtained from training to infer the probability of hit in a binary classification
 265 task. Thus, the responses of LPLC2 units are not directly constrained. It would be interesting to see
 266 whether the outward models can predict the actual activities of biological LPLC2 neurons, such as
 267 those that has been studied systematically by Klapoetke et al *Klapoetke et al. (2017)*.

268 Here, we fed exactly the same set of stimuli used by them to one of the outward filters (256
 269 units) obtained from training on the binary classification task (Fig. 10A). It can be seen that the
 270 model behaves similarly to LPLC2 neurons on many different types of stimuli. The model is selective
 271 to loom signals and does not have strong responses to non-looming ones (Fig. 10B). In addition,
 272 the model in Fig. 10A) can predict response patterns of the real LPLC2 neurons for expanding
 273 bars with different orientations (Fig. 10C, D). However, another outward solution from the same
 274 training procedure (Fig. 1D) predict the patterns in the wide expanding bars differently and out of
 275 phase from the biological data. This shows that even within the outward models, the structures
 276 of biological LPLC2 neurons are only part of the solutions of our model. In Fig. 10E, F), the model
 277 correctly predicts the responses of LPLC2 neurons to various bar expanding stimuli, especially the
 278 inhibitory effects of the inward motions. Moreover, in experiments, it has been found that motion
 279 signals that appear at the periphery of the receptive field will suppress the activities of the LPLC2
 280 neurons (periphery inhibition) (*Klapoetke et al., 2017*), and this phenomenon is also successfully
 281 predicted by the model (Fig. 10G, H) due to the pixels at the top and bottom rows of the inhibitory
 282 filters in Fig. 10A).

283 **Discussion**

284 The radially structured dendrites of the LPLC2 neuron in LP has been suggested to account for this
 285 neuron's response to looming stimuli (*Klapoetke et al., 2017*). Our results show that to understand

286 this unique computational structure, one must take into account the population encoding of
 287 the looming stimuli. For an individual LPLC2 unit, the inward structure makes it a better loom
 288 detector, since it can detect looming objects from more incoming angles 7. As the populations
 289 of the LPLC2 units increases, the outward structures are selected more often than the inward
 290 ones during optimization. The reason for this change is not entirely clear, but intuitively, this is
 291 probably related to the fact that there will be more unit centers within the receptive field of one
 292 unit when the population is larger 6. Neurons work together to perform tasks (*Pasupathy and Connor, 2002*), and population of neurons usually exhibit different and better coding strategies that
 293 cannot be achieved by individual neurons, such as better resolutions in vector coding (*Georgopoulos et al., 1986; Vogels, 1990*) and more robust coding due to correlated noise (*Franke et al., 2016; Zylberberg et al., 2016; Cafaro et al., 2020*). Thus, we emphasize that to understand anatomical,
 294 physiological, and algorithmic properties of individual neurons, one should put it in the context of a
 295 group neurons and consider population coding.

296 Although the outward filter of the LPLC2 unit emerges naturally from the training, one should
 297 not think of it as a learned feature. In fact, the dendritic structure of the LPLC2 neuron is hard wired,
 298 and is shaped through millions of years' evolution [CITATION]. The population size dependence of
 299 the ratio of the outward and inward solutions might be related to some interactions between the
 300 population coding and the computational structures of individual neurons during evolution. For
 301 simpler organism with fewer looming sensitive neurons, and if the neurons rely on motion signals
 302 to detect looming, the inward-like loom computation might be expected. This does not apply to
 303 situations where the looming detectors does not receive any motion information, such as in the
 304 lobula giant motion detector (*Rind and Bramwell, 1996*).

305 Experiments have shown that the LPLC2 neurons are highly selective to looming signals, and
 306 inhibitory circuit play an important role for this selectivity (*Klapoetke et al., 2017*). For example, it
 307 has been found that the motion signals at the periphery of the receptive field of an LPLC2 neuron
 308 inhibit its activity, and this periphery inhibition causes various non-trivial response patterns of the
 309 LPLC2 neurons to different types of stimuli (*Klapoetke et al., 2017*). However, the entire structure of
 310 this inhibitory field is not fully understood (*Klapoetke et al., 2017*). Our model provides a promising
 311 tool to investigate the properties of the inhibitory circuits directly upstream of the LPLC2 neurons.
 312 Specifically, the periphery inhibition structure automatically appears in the biologically-relevant
 313 outward solutions after training, although in our design of the stimuli and the training tasks, there
 314 are no explicit assumptions or requirements about periphery inhibition (Fig. 10). In addition, our
 315 model predicts specific configurations of the inhibitory field that arises to solve the artificial binary
 316 classification tasks (Fig. 6). Combined with more specifically designed experiments, it is possible
 317 that our model could reveal finer properties of this inhibitory field.

318 The LPLC2 units of the outward model exhibits sparsity in their responses to looming stimuli,
 319 contrary to the dense representations in the non-biological inward model (Fig. (8)). During a looming
 320 event, most of the units are quiet and only a few adjacent units have very large activities (*Olshausen and Field, 1997*). It would be interesting to see if this sparse activities could be observed in future
 321 experiments. Since the readout of our model is a summation of the activities of the LPLC2 units,
 322 this sparse properties does not affect the performance of our model and the main results of this
 323 paper. However, we argue that in a different setting, this sparsity might be crucial. For example,
 324 hypothetically, if the LPLC2 conveys the information about the looming directions or angles such as
 325 in some lobula columnar neurons (LC6) (*Morimoto et al., 2020*), then the sparse properties of the
 326 neurons are very important for higher encoding resolutions.

327 In our models, we ignored other types of inputs to LPLC2 neurons such as the ones from the
 328 lobula (*Von Reyn et al., 2017*). It would be interesting to see whether these additional motion
 329 information would have any effect on the trained (LP) filter structures of LPLC2 units. Interestingly,
 330 another lobula columnar neurons (LC4) have their dendrites solely in the lobula, and their axons
 331 projected to the GF (*Von Reyn et al., 2017*). The LPLC2 and LC4 neurons are the only identified
 332 inputs to the GF that mediates the escape behavior of a fly (*Von Reyn et al., 2014; Ache et al.,*

337 **2019**). These parallel channels require a rewritten of the probabilistic model in Eq. (5) where
 338 an additional contributions from LC4 need to be added to the total response. One difficulty of
 339 this model modification is that the computational algorithms of the motion signal integration of
 340 the LPLC2 and LC4 dendrites in the lobula is not entirely clear [CITE]. We leave this for future
 341 investigations.

342 Our model relies on the motion signals to infer the probability of hit, and thus a proper esti-
 343 mation of the motion is crucial. The currently used HRC model 3 could be replaced by a more
 344 sophisticated motion estimator in order to better extract useful information that is conveyed by
 345 the motions of the objects. In a natural environment, the local contrasts fluctuate greatly due to
 346 changing of luminance, occlusions, and other uncontrolled conditions. Thus, a motion detection
 347 model that can adapt to the changing contrast is needed if one applies our model on more realistic
 348 situations (*Drews et al., 2020*). Moreover, the tuning curve of any HRC-type motion estimator
 349 depends on the spacial offset of the inputs and the timescale of the temporal filters. A relevant
 350 quantity here is the R/v ratio, where the R is a size parameter of the object (radius in our case) and
 351 the v is the constant moving velocities. When the R is fixed, the larger the velocity is, the smaller
 352 this ratio will be. We have tried to vary the values of the R/v ratio within different ranges to see how
 353 the nonlinearity of the upstream motion estimation could affect the downstream loom detection
 354 and trained filters, but did not find anything interesting. In our simulations, we keep the ratio in a
 355 range that guarantees that the velocity is within the linear regime of the HRC model (Eq. 3).

356 The ReLU activation function is used in our model any where the nonlinearity is needed. Due to
 357 its simplicity and effectiveness, ReLU is commonly used to build artificial neural network models
 358 (*Glorot et al., 2011*), but whether and how it is relevant in biology especially in the LPLC2 circuit is not
 359 known. However, experimental data have suggested that the LPLC2 neurons might be thresholded,
 360 which means that the sum of the responses of an LPLC2 neuron to parts of the stimuli is smaller
 361 than the response to the whole stimuli (*Klapoetke et al., 2017*). This nonlinearity is consistent with
 362 the behaviors of a ReLU combined with a threshold. We have tried several other types of activation
 363 functions, and found that the main results were not affected, although some activation functions
 364 such as leaky ReLU made the convergence faster.

365 For simplicity, we didn't impose the hexagonal geometry of the ommatidium of the fly eye.
 366 Instead, we assume that visual field is separated into a lattice of 5° squares, with each square
 367 representing a T4/T5 motion detector (Fig. 3). This simplification might alter the geometry of the
 368 trained filters, and potentially affect the reproductions of the LPLC2 responses to various stimuli,
 369 since the specific shapes of the filters matter (Fig. 10). Thus, if one wants to study the dynamics of
 370 the LPLC2 activities, then the hexagonal ommatidium structure might be crucial. However, we don't
 371 think this geometric distinction will affect the main results of the current paper, since we are only
 372 interested in the binary inference problem rather than the LPLC2 activities.

373 Our neural network model is highly constrained by the specific anatomy of the LPLC2 circuits,
 374 and no unnecessary layers are added, which makes the model a shallow neural network (Fig. 1
 375 and Fig. 4). This shallowness leads to the limited dimensionality of our model, which might be
 376 more prone to local minima during training. We have observed that about half of the time, the
 377 training ended up with non-converged filters (e.g., all zeros). This problem could be alleviated by
 378 properly choosing the initialization scales for the filters. However, the ratio of the outward and
 379 inward solutions shown in Fig. 9B is not affected.

380 The simple synthetic stimuli used in this paper can account for a large amount of possible
 381 stimuli that a fly may encounter. However, natural stimuli has been suggested to be very important
 382 to shape the properties of the circuit in retina (*Tanaka et al., 2019*). Thus, adding more complicated
 383 structures in the stimuli is a reasonable next step. For example, a natural environment usually
 384 has a very complex static background, such as grasses, trees or clouds. In addition, there could
 385 be more objects that are moving in the visual field and only some of them are approaching, which
 386 causes distractions. Moreover, looming signals could be corrupted by various kinds of noises, such
 387 as unstable illuminations, occlusions by other objects, intrinsic neural stochasticities, and so forth.

388 It would be interesting to see what effects these more complex stimuli could have on the trained
389 filters and the overall performance.

390 **Methods and Materials**

391 **Code availability**

392 Code to perform all simulations in this paper and to reproduce all figures is available at
 393 <http://www.github.com/ClarkLabCode/XXXXX>.

394 **Coordinate system and stimuli**

395 We designed a suite of visual stimuli to present to our models to simulate looming objects that hit
 396 or miss the fly, retreating objects, and rotational visual fields. In this section, we describe the suite
 397 of stimuli and the coordinate systems used in our simulations.

398 In our simulations and training, the fly sits on a horizontal plane, and its head points towards a
 399 specific direction. The fly head is modeled to be a point particle with no volume. A three dimensional
 400 right-handed frame of reference Σ is set up and attached to the fly head (origin): the z axis points in
 401 the anterior direction from the fly head, perpendicular to the line that connects the two eyes, and
 402 in the horizontal plane of the fly; the y axis points toward the right eye, also in the horizontal plane;
 403 and the x axis points upward and perpendicular to the horizontal plane. Looming or retreating
 404 objects are represented in this space by a sphere with radius $R = 1$, and the coordinates of its
 405 center at time t are denoted as $\mathbf{r}(t) = (x(t), y(t), z(t))$. Thus, the distance between the object center
 406 and the fly head is $D(t) = |\mathbf{r}(t)| = \sqrt{x^2(t) + y^2(t) + z^2(t)}$.

407 Within this coordinate system, we set up cones to represent individual LPLC2 units. The receptive
 408 field of LPLC2 neurons is measured at roughly 60-degree in diameter (*Klapoetke et al., 2017*). Thus,
 409 we here model each LPLC2 unit as a cone with its vertex at the origin and with half-angle of 30
 410 degrees. The orientation of the axis of the cone can be characterized by two of the Euler angles
 411 ψ (around z) and θ (around the new x' axis after the rotation around z) with respect to the frame
 412 of reference. For each LPLC2 unit m ($m = 1, 2, \dots, M$), we set up a local frame of reference Σ_m : the
 413 z_m axis is the axis of the cone and its positive direction points outward from the origin, the x_m axis
 414 lies in the plane spanned by the x axis of Σ and the z_m axis of Σ_m and has an acute angle with the
 415 positive direction of x axis of Σ , and the y_m axis should be chosen such that Σ_m is right-handed. For
 416 each LPLC2 unit, its cardinal directions are defined as: upward (positive direction of x_m), downward
 417 (negative direction of x_m), leftward (negative direction of y_m) and rightward (positive direction of y_m).
 418 To get the signals that are received by a specific LPLC2 unit m , the coordinates of the object in Σ are
 419 rotated to the local frame of reference Σ_m .

420 Within this coordinate system, we can also set up cones representing the extent of a spherical
 421 object moving in the space. The visible outline of a spherical object spans a cone with its point at
 422 the origin. The half-angle of this cone is a function of time and can be denoted as $\theta_s(t)$:

$$\theta_s(t) = \arcsin \frac{R}{D(t)}. \quad (1)$$

423 One may calculate how the cone of the object overlaps with the receptive field cones of each LPLC2
 424 unit.

425 There are multiple layers in the fly visual system (*Takemura et al., 2017*), but here we focus on
 426 only two coarse grained stages of processing: (1) the estimation of local motion direction from
 427 optical intensities by motion detection neurons T4 and T5 and (2) the integration of the flow fields
 428 by LPLC2 neurons. In our simulations, the interior of the m th LPLC2 unit cone is represented by
 429 a N by N matrix, so that each element in this matrix indicates a specific direction in the angular
 430 space within the LPLC2 unit cone. If an element also falls within the object cone, then its value
 431 is set to 1; otherwise it is 0. Thus, at each time t , this matrix is an optical contrast signal and can
 432 be represented by $C(x_m, y_m, t)$, where (x_m, y_m) are the coordinates in Σ_m . In general, N should be
 433 big enough to provide good angular resolutions. Then, K^2 ($K < N$) motion detectors are evenly
 434 distributed within the LPLC2 cone, with each occupying a L by L grid in the N by N matrix, where
 435 $L = N/K$. This L by L grid represents a 5° by 5° square in the angular space, consistent with sizes of
 436 the receptive fields of motion detectors T4/T5 (*Zavatone-Veth et al., 2020*). Since the receptive field

437 of an LPLC2 neuron is roughly 60° , the value of K is set to be 12. To get enough angular resolution
 438 for the local motion detectors, the value of L is set to be 4, and this makes the value of N to be 48.

Each motion detector is assumed to be a Hassenstein Reichardt Correlator (HRC) and calculates local flow fields from $C(x_m, y_m, t)$ (**Hassenstein and Reichardt, 1956**). The HRC used here has two inputs, separated by 5° in the angular space. Each input applies first a spacial filter on the contrast $C(x_m, y_m, t)$ and then temporal filters:

$$I_j(t; x_m, y_m) = \sum_{t'=0}^t \sum_{x'_m=-N}^N \sum_{y'_m=-N}^N f_j(t') G(x'_m, y'_m) C(x_m - x'_m, y_m - y'_m, t - t'), \quad (2)$$

where f_j ($j \in 1, 2$) is a temporal filter and G is a discrete 2d Gaussian kernel with mean 0° and standard deviation of 2.5° to account for the acceptance angle of the fly photoreceptors (**Stavenga, 2003**). For simplicity, the temporal filters f_1 and f_2 were chosen to be two delta functions: $f_1(t') = \delta(t' - (t - \Delta))$ and $f_2 = \delta(t' - t)$, with one peaking with a delay at $t - \Delta$ and the other at the current time t , where Δ was set to 0.03 s (**Salazar-Gatzimas et al., 2016**). With these, we have:

$$F(t; x_{m1}, y_{m1}, x_{m2}, y_{m2}) = I_1(t; x_{m1}, y_{m1}) I_2(t; x_{m2}, y_{m2}) - I_1(t; x_{m2}, y_{m2}) I_2(t; x_{m1}, y_{m1}). \quad (3)$$

439 where $F(t; x_{m1}, y_{m1}, x_{m2}, y_{m2})$ is the local flow fields at time t with two inputs locating at (x_{m1}, y_{m1}) and
 440 (x_{m2}, y_{m2}) , respectively.

In experiment, four types of T5 neurons have been found that project to layers 1, 2, 3, and 4 of the lobula plate. Each type is sensitive to one of the cardinal directions: down, up, left, right (**Maisak et al., 2013**). Thus, in our model, there are four nonnegative, local flow fields that serve as the only inputs to the model: $U_-(t)$ (downward, corresponding LP layer 4), $U_+(t)$ (upward, LP layer 3), $V_-(t)$ (leftward, LP layer 1) and $V_+(t)$ (rightward, LP layer 2), each of which is a K by K matrix. To calculate these matrices by Eq. 3, two sets of motion detectors are needed, one for the vertical directions and one for the horizontal directions. The HRC model in Eq. 3 is direction sensitive and has opponency, which means that for motion in the preferred (null) direction, the output of the HRC model is positive (negative) (**Adelson and Bergen, 1985**). Thus, assuming the upward (rightward) is the preferred vertical (horizontal) direction, we can get the elements of the four flow fields, respectively:

$$\begin{aligned} [U_-(t)]_{k_1 k_2} &= |\min(0, F(t; x_{m1}, y_{m1}, x_{m2}, y_{m2}))| \\ [U_+(t)]_{k_1 k_2} &= |\max(0, F(t; x_{m1}, y_{m1}, x_{m2}, y_{m2}))| \\ [V_-(t)]_{k_1 k_2} &= |\min(0, F(t; x_{m1}, y_{m1}, x_{m2}, y_{m2}))| \\ [V_+(t)]_{k_1 k_2} &= |\max(0, F(t; x_{m1}, y_{m1}, x_{m2}, y_{m2}))|, \end{aligned}$$

441 where $k_1, k_2 \in \{1, 2, \dots, K\}$ and $|\cdot|$ represents the absolute value. In the above expressions, it implies,
 442 for $[U_-(t)]_{k_1 k_2}$ and $[U_+(t)]_{k_1 k_2}$, the vertical motion detector at (k_1, k_2) has its two inputs located at
 443 (x_{m1}, y_{m1}) and (x_{m2}, y_{m2}) , respectively. Similarly, for $[V_-(t)]_{k_1 k_2}$ and $[V_+(t)]_{k_1 k_2}$, the horizontal motion
 444 detector at (k_1, k_2) has its two inputs located at (x_{m1}, y_{m1}) and (x_{m2}, y_{m2}) .

445 We simulated the trajectories $\mathbf{r}(t)$ of the object in the frame of reference Σ with a time resolution
 446 of 0.01 s. For hit, miss, and retreat cases, the trajectories of the object are always straight lines (i.e.,
 447 ballistic motion), and the velocities of the object were randomly sampled from a range $[2R, 10R](s^{-1})$
 448 and all the trajectories are confined to be within a sphere of $5R$ (All figures except Fig. 1C) or $10R$
 449 (Fig. 1C) (**Supplementary figures are not referenced correctly.**) centered at the fly head. The radius
 450 of the object, R , was always set to be 1. To generate rotational stimuli, we placed 100 objects at
 451 random positions around the fly, and rotated them all about a specific axis certain axis. The rotation
 452 speed was chosen from a Gaussian distribution with a mean $0^\circ/s$ and standard deviation $200^\circ/s$, a
 453 reasonable rotational velocity for walking flies (**DeAngelis et al., 2019**).

454 **Models**

455 Experiments have shown that an LPLC2 neuron has four dendritic structures in the four LP layers,
 456 and that they receive direct excitatory inputs from T4/T5 motion detection neurons (*Maisak et al., 2013; Klapoetke et al., 2017*). Besides, it has been proposed that each dendritic structure also
 457 receive inhibitory inputs mediated by lobulate plate intrinsic interneurons, such as LPi4-3 (*Klapoetke
 et al., 2017*). Thus, our models have two types of nonnegative filters, one excitatory and one
 458 inhibitory (Fig. 4), represented by W^e and W^i , respectively. Each filter is a 12 by 12 matrix. Next,
 459 we rotate counterclockwise W^e and W^i by multiples of 90° to obtain the filters that are used to
 460 integrate the four motion signals: $U_-(t)$, $U_+(t)$, $V_-(t)$, $V_+(t)$. Specifically, we define the corresponding
 461 four excitatory filters as: $W_{U_-}^e = \text{rotate}(W^e, 270^\circ)$, $W_{U_+}^e = \text{rotate}(W^e, 90^\circ)$, $W_{V_-}^e = \text{rotate}(W^e, 180^\circ)$,
 462 $W_{V_+}^e = \text{rotate}(W^e, 0^\circ)$, and the inhibitory filters as: $W_{U_-}^i = \text{rotate}(W^i, 270^\circ)$, $W_{U_+}^i = \text{rotate}(W^i, 90^\circ)$,
 463 $W_{V_-}^i = \text{rotate}(W^i, 180^\circ)$, $W_{V_+}^i = \text{rotate}(W^i, 0^\circ)$. In addition, we impose mirror symmetry to the filters,
 464 and with the above definitions of the rotated filters, the upper half of W^e is a mirror image of the lower
 465 half of W^e . The same mirror symmetry also applies to W^i . Thus, there are in total 144 parameters
 466 in the two sets of filters. In fact, since only the elements within a 60 degree cone contribute to the
 467 filter for the LPLC2 units, the corners are neglected, and there are only 112 trainable parameters in
 468 the excitatory and inhibitory filters.

469 In computer simulations, the weights and flow fields are flattened to be one-dimensional column
 470 vectors. The responses of the inhibitory units are:

$$\begin{aligned} r_{U_-}^i(t) &= \phi \left[(W_{U_-}^i)^T U_-(t) + b^i \right] \\ r_{U_+}^i(t) &= \phi \left[(W_{U_+}^i)^T U_+(t) + b^i \right] \\ r_{V_+}^i(t) &= \phi \left[(W_{V_+}^i)^T V_+(t) + b^i \right] \\ r_{V_-}^i(t) &= \phi \left[(W_{V_-}^i)^T V_-(t) + b^i \right], \end{aligned}$$

471 where $\phi(\cdot) = \max(\cdot, 0)$ is the rectified linear activation function, and $b^i \in \mathbb{R}$ is the intercept.

The response of a single LPLC2 unit m is:

$$r_m(t) = \phi \left[(W_{U_-}^e)^T U_-(t) + (W_{U_+}^e)^T U_+(t) + (W_{V_+}^e)^T V_+(t) + (W_{V_-}^e)^T V_-(t) - (r_{U_-}^i(t) + r_{U_+}^i(t) + r_{V_+}^i(t) + r_{V_-}^i(t)) + b^e \right], \quad (4)$$

472 where $b^e \in \mathbb{R}$ is the intercept (4).

473 The inferred probability of hit for a specific trajectory is:

$$\hat{P}_{\text{hit}} = \frac{1}{T} \sum_{t=1}^T \sigma \left(\sum_m r_m(t) + b \right), \quad (5)$$

474 where T is the total time steps of the trajectory and $\sigma(\cdot)$ is the sigmoid function. Since we are adding
 475 three intercepts b^i, b^e , and b , there are 115 parameters to train in this model.

476 There are some variations of the above model that have also been tested. The first variation
 477 introduces a modified probability model compared with Eq. 5:

$$\hat{P}'_{\text{hit}} = \frac{1}{T} \sum_{t=1}^T \left[2\sigma \left(\sum_m r_m(t) \right) - 1 \right]. \quad (6)$$

478 A second variation we tested is a modification of Eq. (4), where the inhibitory units are deleted
 479 and the filters, represented by $W'_{U_-}, W'_{U_+}, W'_{V_+}, W'_{V_-}$, are allowed to have both positive and negative
 480 values, i.e.,

$$r'_m(t) = \phi \left[(W'_{U_-})^T U_-(t) + (W'_{U_+})^T U_+(t) + (W'_{V_+})^T V_+(t) + (W'_{V_-})^T V_-(t) + b' \right]. \quad (7)$$

481 **Training and testing**

482 We created a synthetic data set containing four types of motions: *loom-and-hit*, *loom-and-miss*,
 483 *retreat*, and *rotation*. The proportions of these types were 0.25, 0.125, 0.125, 0.5 respectively. In
 484 total, there were 5200 trajectories, with 4,000 for training and 1,200 for testing. Trajectories with
 485 motion type *loom-and-hit* are labeled as hit or $y_n = 1$ (probability of hit is 1), while trajectories of
 486 other motion types are labeled as non-hit or $y_n = 0$ (probability of hit is 0), where n is the index of
 487 each specific sample.

488 The loss function to be minimized in our training was the cross entropy between the label y_n
 489 and the inferred probability of hit \hat{P}_{hit} , and averaged across all samples, plus a regularization term:

$$\text{loss} = -\frac{1}{N} \sum_{n=1}^N \left[y_n \log \hat{P}_{\text{hit}}(n) + (1 - y_n) \log(1 - \hat{P}_{\text{hit}}(n)) \right] + \beta \sum_W \|W\|^2, \quad (8)$$

490 where $\hat{P}_{\text{hit}}(n)$ is the inferred probability of hit for sample n , β is the strength of an L2 regularization,
 491 and W represents all the effective parameters in the two excitatory and inhibitory filters.

492 The strength of the regularization β was set to be 10^{-4} , which was obtained by gradually increasing
 493 β until the performance of the model on test data started to drop. The regularization sped up
 494 convergence of solutions, but the regularization strength did not strongly influence the main results
 495 in the paper, as long as it was not too strong, that is, as long as it was much less than 1.

496 To speed up training, rather than taking a temporal average as shown in Eq. (5), a snapshot
 497 was sampled randomly from each trajectory, and the probability of hit of this snapshot was used
 498 to represent the whole trajectory, i.e., $\hat{P}_{\text{hit}} = \sigma(\sum_m r_m(t) + b)$, where t is a random sample from
 499 $\{1, 2, \dots, T\}$. Mini-batch gradient descent was used in training, and the learning rate was 0.001.

500 After training, the models were tested on the entire trajectories with the probability of hit
 501 defined in Eq. (5). Models trained only on snapshots data performed very well on the test data.
 502 During testing, the performance of the model was evaluated by the area under the curve (AUC)
 503 of the receiver operating characteristic (ROC) and precision-recall (PR) curves (Hanley and McNeil,
 504 1982; Davis and Goadrich, 2006).

505 TensorFlow (Abadi et al., 2016) was used to train all models.

506 **Clustering the solutions**

507 To cluster the solutions, we used the following procedure. Each solution had an excitatory and an
 508 inhibitory filter. We flattened these two filters, and concatenated them into a single vector. (The
 509 elements at the corners were deleted since they are outside of the receptive field.) Thus, each
 510 solution was represented by a vector, from which we calculated the cosine distance for each pair
 511 of solutions. The obtained distance matrix was then fed into a hierarchical clustering algorithm
 512 (Virtanen et al., 2020). After obtaining the hierarchical clustering, the outward and inward filters
 513 were identified by their shape. We summed the element values of filter corresponding to flow with
 514 components radiating outwards and subtracted the values of the filter corresponding to flow with
 515 components directed inwards. If this sum was positive, then the filters were labeled as outward;
 516 otherwise, the filters were labeled as inward. If the elements in the concatenated vector are all
 517 close to zero, then the corresponding filters were labeled as unstructured.

518 **Statistics**

519 For a model with M LPLC2 units, where $M \in \{1, 2, 4, 8, 16, 32, 64, 128, 192, 256\}$, 200 random initializa-
 520 tions were used to train it. Within these 200 trainings, the numbers of outward solutions N_{out} are
 521 (starting from smaller M's): 33, 44, 42, 46, 50, 49, 51, 50, 49, 46 (out of 150), and the numbers of
 522 inward solutions N_{in} are: 70, 67, 68, 67, 66, 64, 60, 33, 27, 12 (out of 150). The average score curves
 523 and dots in Fig. 9A) were obtained by taking average among each type of solutions, respectively,
 524 and the shades indicate one standard deviation. The curve and dots in Fig. 9B) are the ratio of
 525 the number of outward solutions to the number of inward solutions. To obtain the error bar (grey
 526 shade), we considered the training results as a binomial distribution, with the probability to get

527 the outward solutions being $N_{\text{out}}/(N_{\text{out}} + N_{\text{in}})$, and the inward being $N_{\text{in}}/(N_{\text{out}} + N_{\text{in}})$. Thus, the
 528 standard deviation of this binomial distribution is $\sigma_b = \sqrt{N_{\text{out}}N_{\text{in}}/(N_{\text{out}} + N_{\text{in}})}$, which should be on
 529 both N_{out} and N_{in} . From this, we can calculate the error bar as the propagated error:

$$\text{propagated error} = \frac{N_{\text{out}}}{N_{\text{in}}} \sqrt{\left(\frac{\sigma_b}{N_{\text{out}}}\right)^2 + \left(\frac{\sigma_b}{N_{\text{in}}}\right)^2}. \quad (9)$$

530 Acknowledgments

531 We thank ...

532 References

- 533 **Abadi M**, Barham P, Chen J, Chen Z, Davis A, Dean J, Devin M, Ghemawat S, Irving G, Isard M, et al. Tensorflow:
 534 A system for large-scale machine learning. In: *12th {USENIX} symposium on operating systems design and*
 535 *implementation ({OSDI} 16)*; 2016. p. 265–283.
- 536 **Ache JM**, Polksy J, Alghailani S, Parekh R, Breads P, Peek MY, Bock DD, von Reyn CR, Card GM. Neural basis
 537 for looming size and velocity encoding in the Drosophila giant fiber escape pathway. *Current Biology*. 2019;
 538 29(6):1073–1081.
- 539 **Adelson EH**, Bergen JR. Spatiotemporal energy models for the perception of motion. *Josa a*. 1985; 2(2):284–299.
- 540 **Ball W**, Tronick E. Infant responses to impending collision: Optical and real. *Science*. 1971; 171(3973):818–820.
- 541 **Bhattacharyya K**, McLean DL, MacIver MA. Visual threat assessment and reticulospinal encoding of calibrated
 542 responses in larval zebrafish. *Current Biology*. 2017; 27(18):2751–2762.
- 543 **Cafaro J**, Zylberberg J, Field GD. Global motion processing by populations of direction-selective retinal ganglion
 544 cells. *Journal of Neuroscience*. 2020; 40(30):5807–5819.
- 545 **Card G**, Dickinson MH. Visually mediated motor planning in the escape response of Drosophila. *Current Biology*.
 546 2008; 18(17):1300–1307.
- 547 **Davis J**, Goadrich M. The relationship between Precision-Recall and ROC curves. In: *Proceedings of the 23rd*
 548 *international conference on Machine learning*; 2006. p. 233–240.
- 549 **De Vries SE**, Clandinin TR. Loom-sensitive neurons link computation to action in the Drosophila visual system.
 550 *Current Biology*. 2012; 22(5):353–362.
- 551 **DeAngelis BD**, Zavatone-Veth JA, Clark DA. The manifold structure of limb coordination in walking Drosophila.
 552 *Elife*. 2019; 8:e46409.
- 553 **Drews MS**, Leonhardt A, Pirogova N, Richter FG, Schuetzenberger A, Braun L, Serbe E, Borst A. Dynamic signal
 554 compression for robust motion vision in flies. *Current Biology*. 2020; 30(2):209–221.
- 555 **Dunn TW**, Gebhardt C, Naumann EA, Riegler C, Ahrens MB, Engert F, Del Bene F. Neural circuits underlying
 556 visually evoked escapes in larval zebrafish. *Neuron*. 2016; 89(3):613–628.
- 557 **Franke F**, Fiscella M, Sevelev M, Roska B, Hierlemann A, da Silveira RA. Structures of neural correlation and how
 558 they favor coding. *Neuron*. 2016; 89(2):409–422.
- 559 **Gabbiani F**, Krapp HG, Laurent G. Computation of object approach by a wide-field, motion-sensitive neuron.
 560 *Journal of Neuroscience*. 1999; 19(3):1122–1141.
- 561 **Georgopoulos AP**, Schwartz AB, Kettner RE. Neuronal population coding of movement direction. *Science*. 1986;
 562 233(4771):1416–1419.
- 563 **Glorot X**, Bordes A, Bengio Y. Deep sparse rectifier neural networks. In: *Proceedings of the fourteenth international*
 564 *conference on artificial intelligence and statistics* JMLR Workshop and Conference Proceedings; 2011. p. 315–323.
- 565 **Hanley JA**, McNeil BJ. The meaning and use of the area under a receiver operating characteristic (ROC) curve.
 566 *Radiology*. 1982; 143(1):29–36.
- 567 **Hassenstein B**, Reichardt W. Systemtheoretische analyse der zeit-, reihenfolgen-und vorzeichenauswertung
 568 bei der bewegungsperzeption des rüsselkäfers chlorophanus. *Zeitschrift für Naturforschung B*. 1956; 11(9–
 569 10):513–524.

- 570 **Hervais-Adelman A**, Legrand LB, Zhan M, Tamietto M, de Gelder B, Pegna AJ. Looming sensitive cortical
571 regions without V1 input: evidence from a patient with bilateral cortical blindness. *Frontiers in integrative*
572 *neuroscience*. 2015; 9:51.
- 573 **King SM**, Dykeman C, Redgrave P, Dean P. Use of a distracting task to obtain defensive head movements to
574 looming visual stimuli by human adults in a laboratory setting. *Perception*. 1992; 21(2):245–259.
- 575 **Klapoetke NC**, Nern A, Peek MY, Rogers EM, Breads P, Rubin GM, Reiser MB, Card GM. Ultra-selective looming
576 detection from radial motion opponency. *Nature*. 2017; 551(7679):237–241.
- 577 **Liu YJ**, Wang Q, Li B. Neuronal responses to looming objects in the superior colliculus of the cat. *Brain, Behavior*
578 *and Evolution*. 2011; 77(3):193–205.
- 579 **Maisak MS**, Haag J, Ammer G, Serbe E, Meier M, Leonhardt A, Schilling T, Bahl A, Rubin GM, Nern A, et al. A
580 directional tuning map of *Drosophila* elementary motion detectors. *Nature*. 2013; 500(7461):212–216.
- 581 **Mauss AS**, Pankova K, Arenz A, Nern A, Rubin GM, Borst A. Neural circuit to integrate opposing motions in the
582 visual field. *Cell*. 2015; 162(2):351–362.
- 583 **Morimoto MM**, Nern A, Zhao A, Rogers EM, Wong AM, Isaacson MD, Bock DD, Rubin GM, Reiser MB. Spatial
584 readout of visual looming in the central brain of *Drosophila*. *Elife*. 2020; 9:e57685.
- 585 **Muijres FT**, Elzinga MJ, Melis JM, Dickinson MH. Flies evade looming targets by executing rapid visually directed
586 banked turns. *Science*. 2014; 344(6180):172–177.
- 587 **Münch TA**, Da Silveira RA, Siegert S, Viney TJ, Awatramani GB, Roska B. Approach sensitivity in the retina
588 processed by a multifunctional neural circuit. *Nature neuroscience*. 2009; 12(10):1308–1316.
- 589 **Oliva D**, Tomsic D. Computation of object approach by a system of visual motion-sensitive neurons in the crab
590 *Neohelice*. *Journal of neurophysiology*. 2014; 112(6):1477–1490.
- 591 **Olshausen BA**, Field DJ. Sparse coding with an overcomplete basis set: A strategy employed by V1? *Vision*
592 *research*. 1997; 37(23):3311–3325.
- 593 **Pasupathy A**, Connor CE. Population coding of shape in area V4. *Nature neuroscience*. 2002; 5(12):1332–1338.
- 594 **Regan D**, Beverley K. Looming detectors in the human visual pathway. *Vision research*. 1978; 18(4):415–421.
- 595 **Rind FC**, Bramwell D. Neural network based on the input organization of an identified neuron signaling
596 impending collision. *Journal of neurophysiology*. 1996; 75(3):967–985.
- 597 **Salay LD**, Ishiko N, Huberman AD. A midline thalamic circuit determines reactions to visual threat. *Nature*.
598 2018; 557(7704):183–189.
- 599 **Salazar-Gatzimas E**, Chen J, Creamer MS, Mano O, Mandel HB, Matulis CA, Pottackal J, Clark DA. Direct
600 measurement of correlation responses in *Drosophila* elementary motion detectors reveals fast timescale
601 tuning. *Neuron*. 2016; 92(1):227–239.
- 602 **Santer RD**, Simmons PJ, Rind FC. Gliding behaviour elicited by lateral looming stimuli in flying locusts. *Journal*
603 *of Comparative Physiology A*. 2005; 191(1):61–73.
- 604 **Sato K**, Yamawaki Y. Role of a looming-sensitive neuron in triggering the defense behavior of the praying mantis
605 *Tenodera aridifolia*. *Journal of neurophysiology*. 2014; 112(3):671–682.
- 606 **Shang C**, Liu Z, Chen Z, Shi Y, Wang Q, Liu S, Li D, Cao P. A parvalbumin-positive excitatory visual pathway to
607 trigger fear responses in mice. *Science*. 2015; 348(6242):1472–1477.
- 608 **Stavenga D**. Angular and spectral sensitivity of fly photoreceptors. II. Dependence on facet lens F-number and
609 rhabdomere type in *Drosophila*. *Journal of Comparative Physiology A*. 2003; 189(3):189–202.
- 610 **Sun H**, Frost BJ. Computation of different optical variables of looming objects in pigeon nucleus rotundus
611 neurons. *Nature neuroscience*. 1998; 1(4):296–303.
- 612 **Takemura Sy**, Nern A, Chklovskii DB, Scheffer LK, Rubin GM, Meinertzhagen IA. The comprehensive connectome
613 of a neural substrate for 'ON'motion detection in *Drosophila*. *Elife*. 2017; 6:e24394.
- 614 **Tanaka H**, Nayebi A, Maheswaranathan N, McIntosh L, Baccus SA, Ganguli S. From deep learning to mechanistic
615 understanding in neuroscience: the structure of retinal prediction. *arXiv preprint arXiv:191206207*. 2019; .

- 616 **Temizer I**, Donovan JC, Baier H, Semmelhack JL. A visual pathway for looming-evoked escape in larval zebrafish.
617 Current Biology. 2015; 25(14):1823–1834.
- 618 **Virtanen P**, Gommers R, Oliphant TE, Haberland M, Reddy T, Cournapeau D, Burovski E, Peterson P, Weckesser
619 W, Bright J, van der Walt SJ, Brett M, Wilson J, Millman KJ, Mayorov N, Nelson ARJ, Jones E, Kern R, Larson E,
620 Carey CJ, et al. SciPy 1.0: Fundamental Algorithms for Scientific Computing in Python. Nature Methods. 2020;
621 17:261–272. doi: 10.1038/s41592-019-0686-2.
- 622 **Vogels R**. Population coding of stimulus orientation by striate cortical cells. Biological cybernetics. 1990;
623 64(1):25–31.
- 624 **Von Reyn CR**, Breads P, Peek MY, Zheng GZ, Williamson WR, Yee AL, Leonardo A, Card GM. A spike-timing
625 mechanism for action selection. Nature neuroscience. 2014; 17(7):962.
- 626 **Von Reyn CR**, Nern A, Williamson WR, Breads P, Wu M, Namiki S, Card GM. Feature integration drives probabilistic
627 behavior in the *Drosophila* escape response. Neuron. 2017; 94(6):1190–1204.
- 628 **Wu LQ**, Niu YQ, Yang J, Wang SR. Tectal neurons signal impending collision of looming objects in the pigeon.
629 European Journal of Neuroscience. 2005; 22(9):2325–2331.
- 630 **Wu M**, Nern A, Williamson WR, Morimoto MM, Reiser MB, Card GM, Rubin GM. Visual projection neurons in the
631 *Drosophila* lobula link feature detection to distinct behavioral programs. Elife. 2016; 5:e21022.
- 632 **Yilmaz M**, Meister M. Rapid innate defensive responses of mice to looming visual stimuli. Current Biology. 2013;
633 23(20):2011–2015.
- 634 **Zavatone-Veth JA**, Badwan BA, Clark DA. A minimal synaptic model for direction selective neurons in *Drosophila*.
635 Journal of vision. 2020; 20(2):2–2.
- 636 **Zylberberg J**, Cafaro J, Turner MH, Shea-Brown E, Rieke F. Direction-selective circuits shape noise to ensure a
637 precise population code. Neuron. 2016; 89(2):369–383.

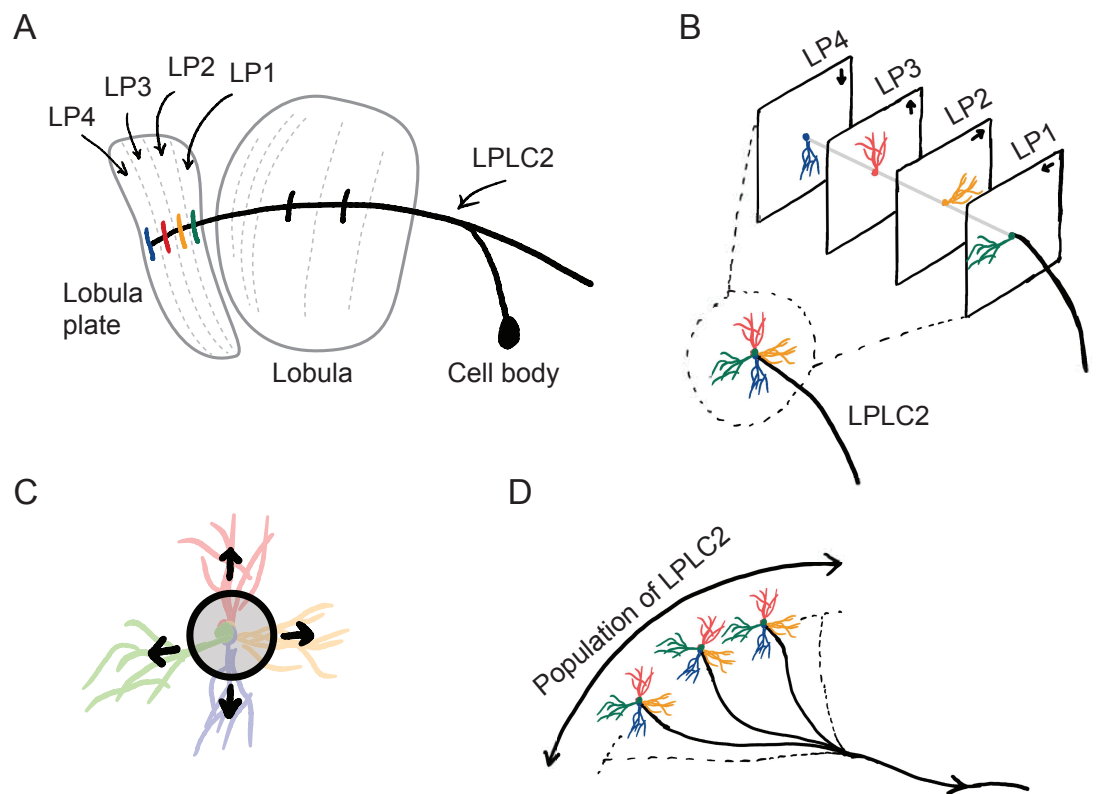


Figure 1. Sketches of the anatomical structures of LPLC2 neurons. (A) An LPLC2 neuron has dendrites in lobula and the four layers of the lobula plate (LP): LP1, LP2, LP3 and LP4. (B) The schematics of the four branches of the LPLC2 dendrites in the four layers of the LP. The arrows indicate the cardinal directions of the corresponding LP layers, which receive motion signals from motion detection neurons. (C) The outward dendritic structure of an LPLC2 neuron coincides with the expanding edges of a looming object (black circle). (D) A population of LPLC2 neurons (over 200) converge their axons to the giant fiber, a descending neuron, to contribute to escaping behaviors.

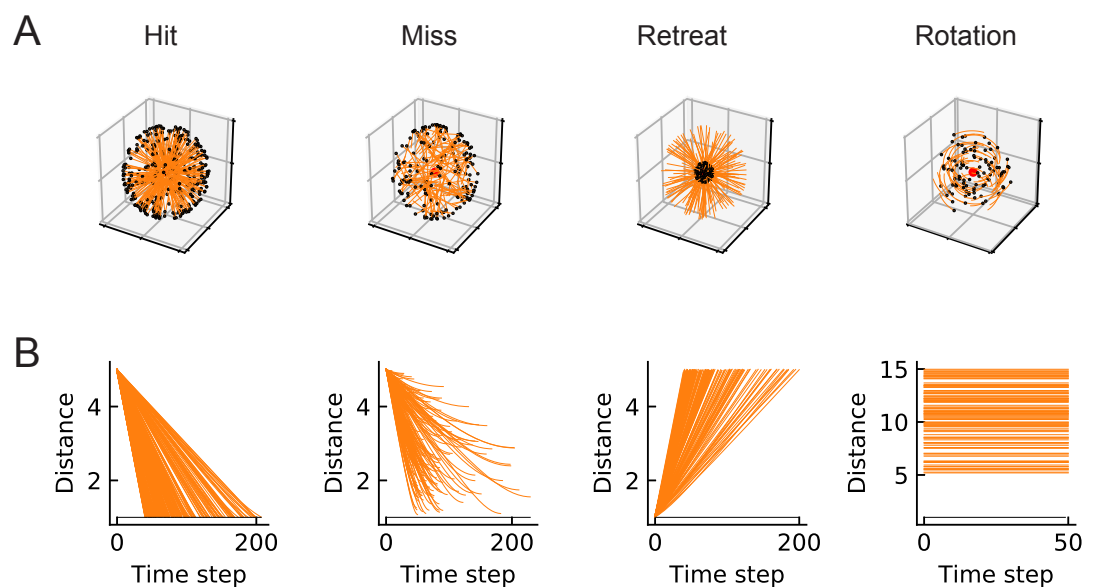


Figure 2. Four types of synthetic stimuli. (A) Orange lines represent trajectories of the stimuli. The black dots represent the starting points of the trajectories. For hit, miss, and retreat cases, multiple trajectories are shown. For rotation, only one trajectory is shown. (B) Distances of the objects to the fly eye as a function of time step.

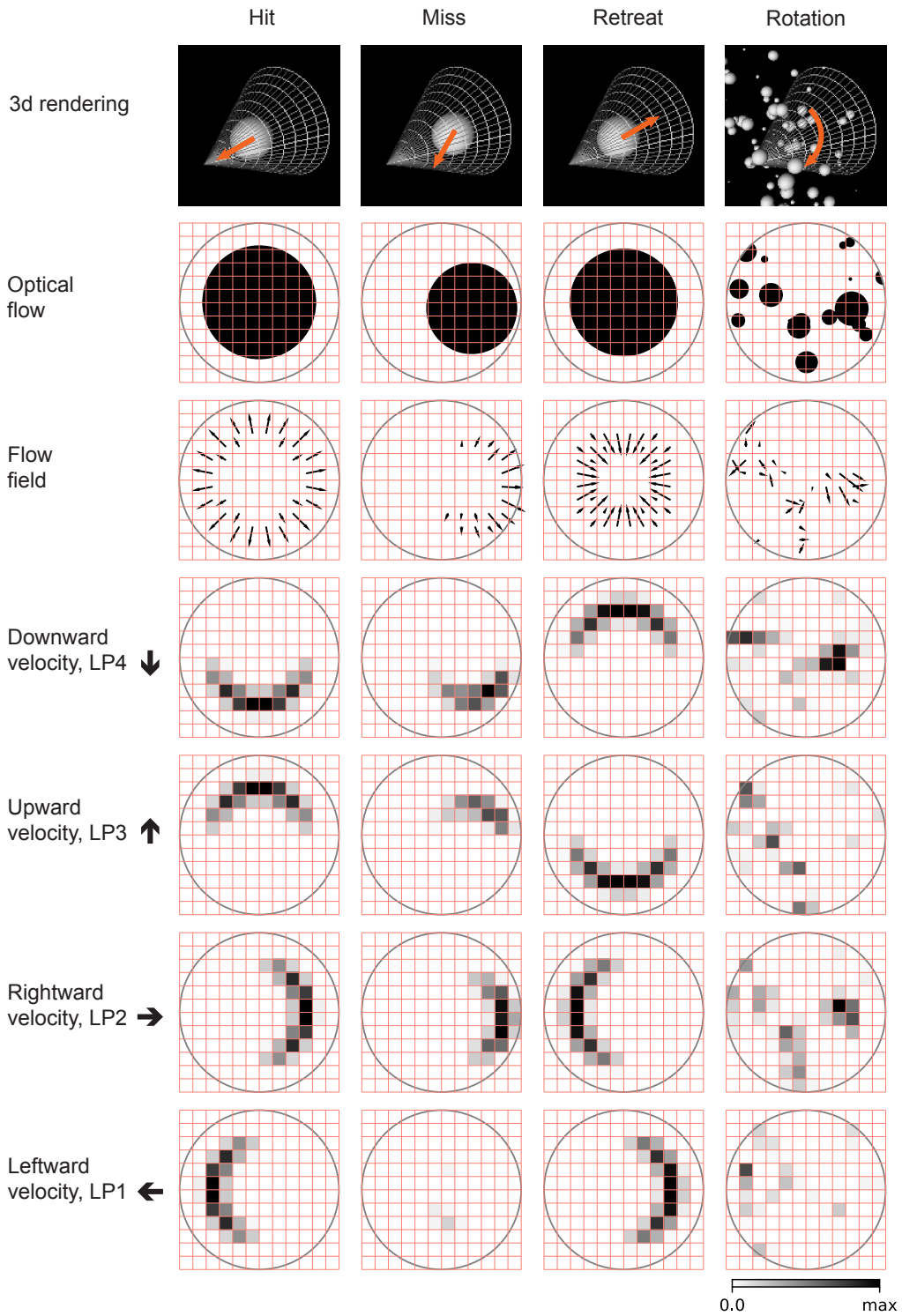


Figure 3. Corresponding to Fig. 2), snapshots of optical flows and flow fields calculated by a Hassenstein Reichardt correlator (HRC) model. First row: 3d rendering of the spherical objects and the LPLC2 receptive field (the cones) at a specific time step. The orange arrows indicate the moving directions of the objects. Second row: 2d projections of the objects (black shades) within the LPLC2 receptive field (the grey circles). Third row: the thin black arrows indicate flow fields generated by the edges of the moving objects. Forth to seventh rows: decomposition of the flow fields in the four cardinal directions with respect to the LPLC2 neuron under consideration: downward, upward, rightward, and leftward, as indicated by the thick black arrows.

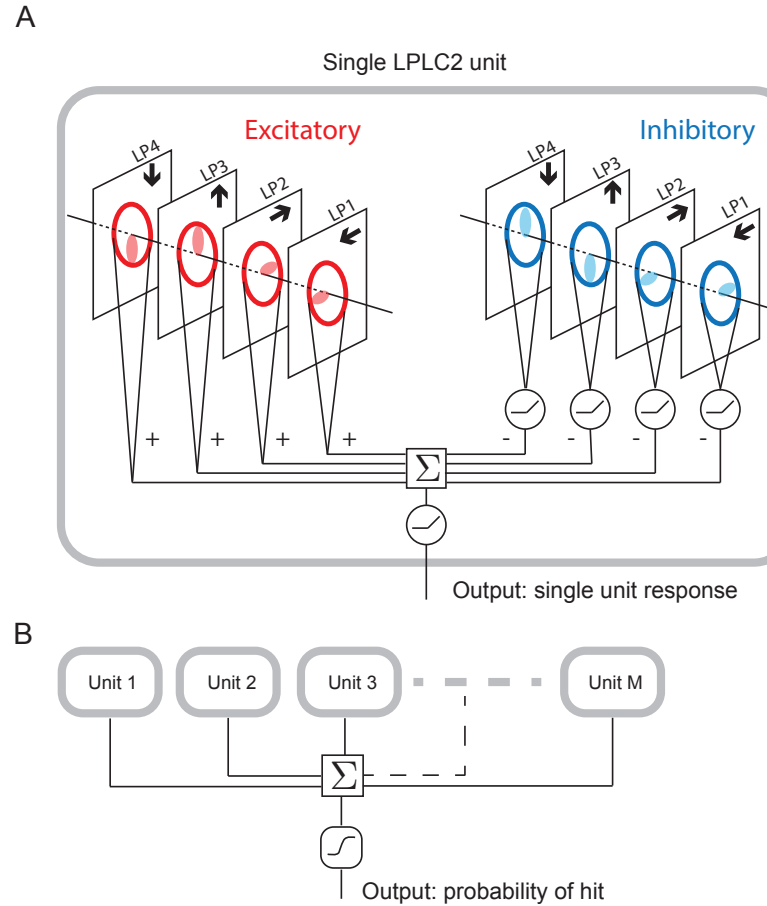


Figure 4. Schematic of the model. (A) Single LPLC2 unit. There are two sets of nonnegative filters: excitatory (red) and inhibitory (blue). Each set of filters has four branches, and each branch receives motion signals (forth to seventh rows in Fig. 3) from the corresponding layer of the LP. The integrated signals from the excitatory branches and the inhibitory branches (rectified) are pooled together to go through a rectifier to produce an output, which is the response of a single LPLC2 unit. Each inhibitory input goes through a rectifier before pooled. (B) The outputs from M LPLC2 units are summed and fed into a sigmoid function to generate the probability of hit. (C) The M LPLC2 units have their orientations almost evenly distributed in the angular space. Red dots and lines represent the centers of the receptive fields and the grey lines represent the boundaries of the receptive fields.

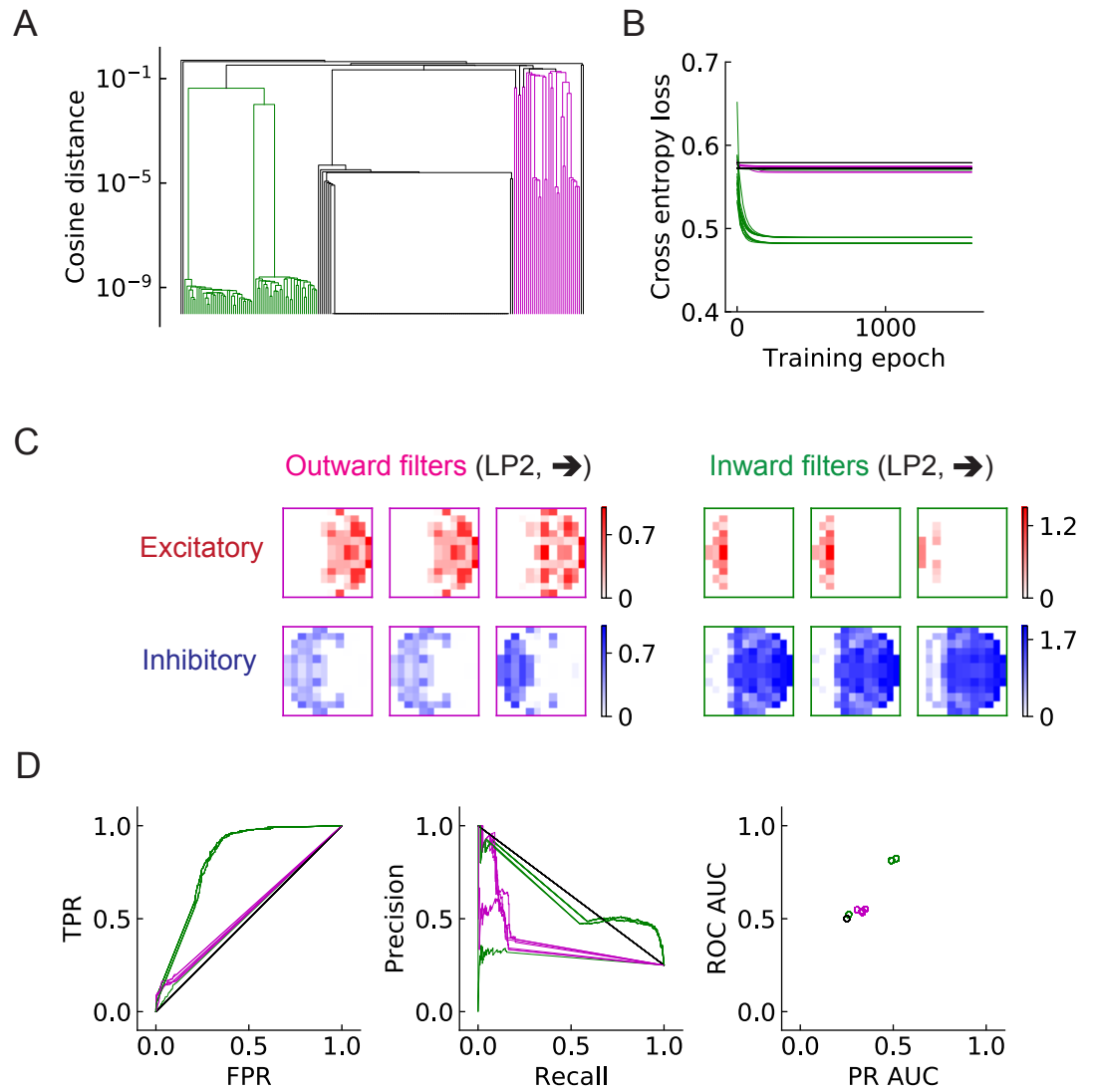


Figure 5. Two distinct types of models appear from training a single LPC2 unit on the binary classification task. (A) Clustering of the trained filters/weights shown as a dendrogram. Different colors indicate different clusters, which are preserved for the rest of the paper. (B) The trajectories of the loss functions during training. (C) The two distinct types of models are represented by two types of filters that are exactly the opposite to each other: outward model (magenta) and inward model (green). The excitatory filters are shown as red, and the inhibitory filters are shown as blue. (D) Performances of the two models. TPR: true positive rate; FPR: false positive rate; ROC: receiver operating characteristic; PR: precision recall; AUC: area under the curve.

Figure 5-Figure supplement 1. More examples of the trained filters for the two types of models and the inferred probability of hit for the four types synthetic stimuli.

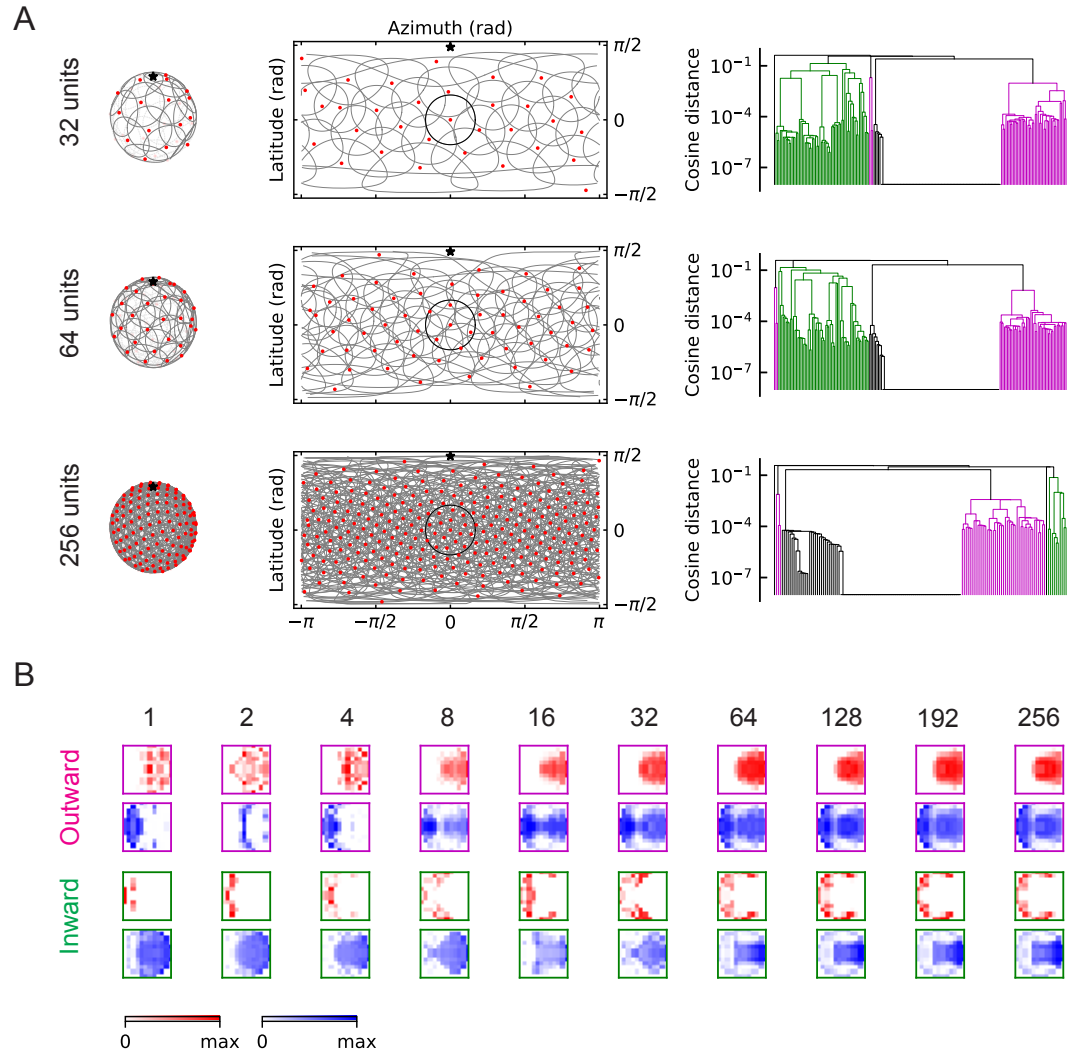


Figure 6. The outward and inward models also appear for models with multiple LPLC2 units. (A) Left column: angular distributions of the LPLC2 units, where red dots are centers of the receptive fields, the grey circles are the boundaries of the receptive field and the black star shows the top of the fly head. Middle column: 2d mapping of the LPLC2 units with symbols being the same as in the left column. Right column: clustering results shown as dendograms with color codes the same as in Fig. 5A). (B) Examples of the trained excitatory/inhibitory filters for outward and inward models with different numbers of LPLC2 units.

Figure 6-Figure supplement 1. Performance of the models.

Figure 6-Figure supplement 2. More examples of the outward filters.

Figure 6-Figure supplement 3. More examples of the inward filters.

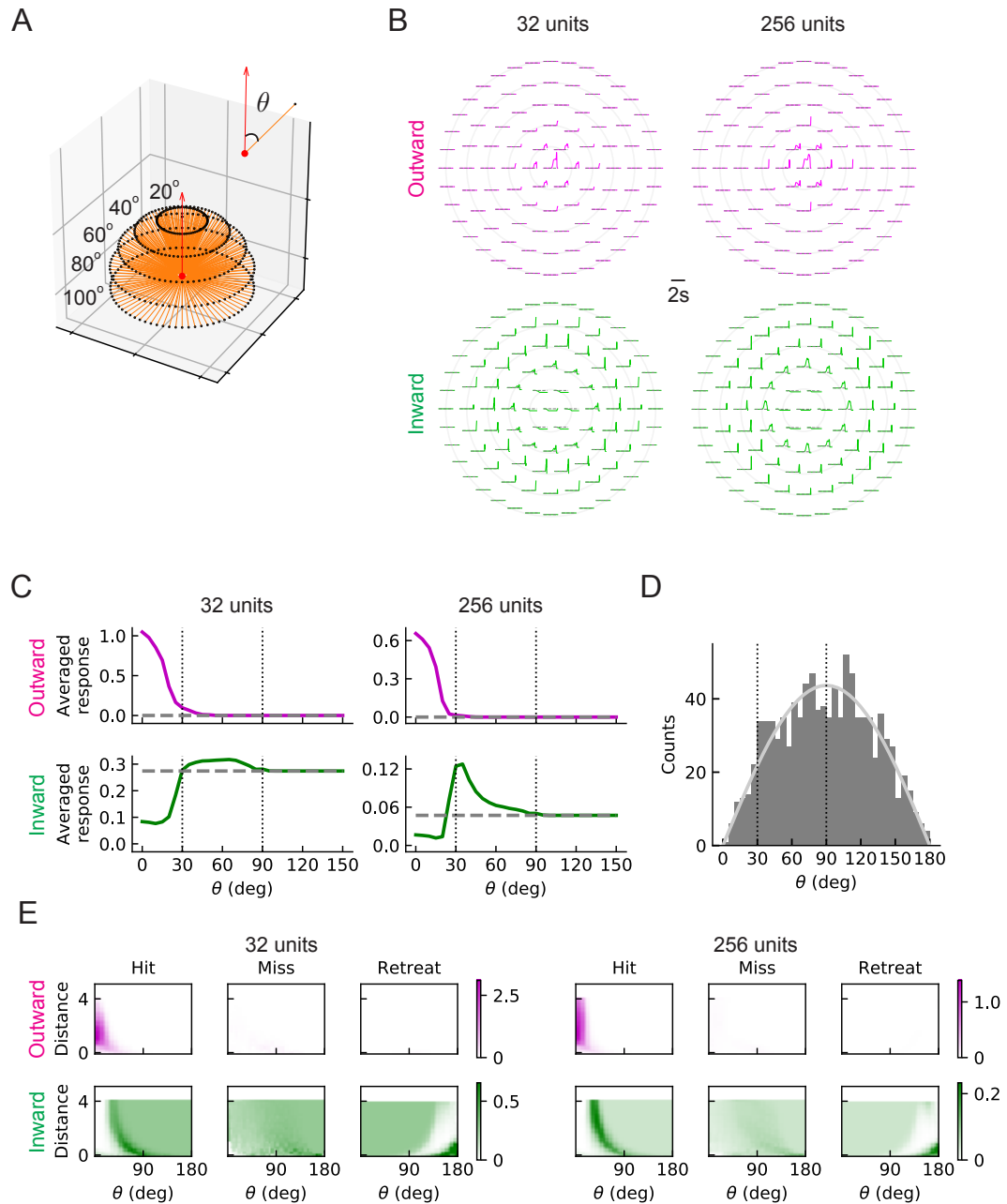


Figure 7. The outward and inward filters show distinct behaviors: single unit analysis. (A) Trajectories of hit stimuli with different incoming angles θ . Symbols are the same as in Fig. 2) except that the upward red arrow represents the orientation of one LPLC2 unit. The numbers with degree unit indicate the specific values of the incoming angles. (B) Response patterns of a single LPLC2 unit with either outward (magenta) or inward (green) filters obtained from models with 32 and 256 units, respectively. The grey dashed lines show the baseline activity of the unit when there is no stimulus. The solid grey concentric circles correspond to the values of the incoming angles in (A). (C) Temporally averaged responses against the incoming angle θ . Symbols and color codes are the same as in (B). (D) Histogram of the incoming angles for the hit stimuli in Fig. 2A). The grey curve represents a rescaled sine wave with half of the period. (E) Heatmaps of the responses of a single LPLC2 unit against the incoming angle θ and the distance to the fly head, for both outward and inward filters obtained from models with 32 and 256 units, respectively.

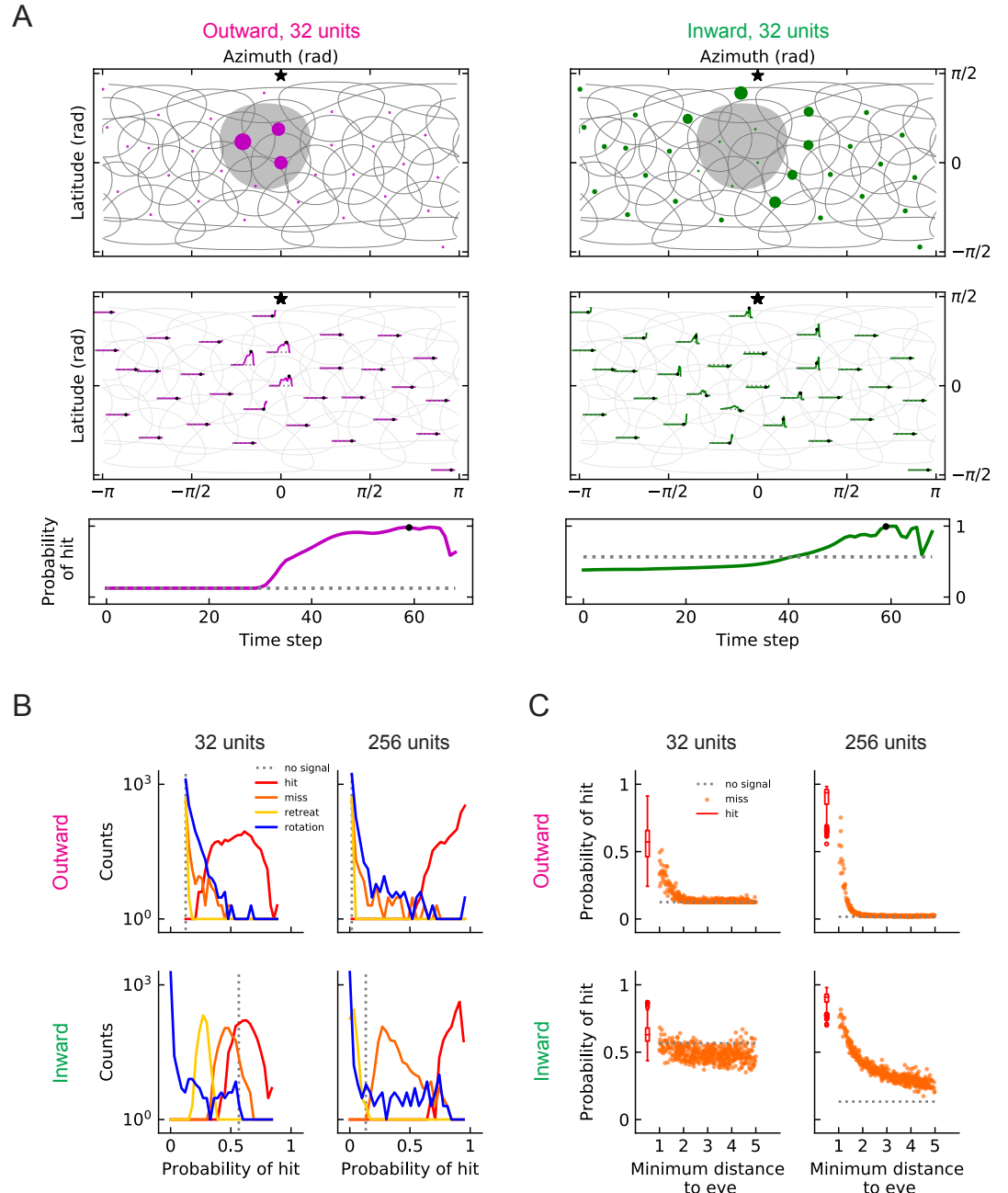


Figure 8. Population coding. (A) Top row: a snapshot of the responses of the outward LPLC2 units (magenta dots) for a hitting object (grey shade). Symbols and color codes are the same as in Fig. 6A). Middle row: the whole trajectories of the responses for the same hitting object as in the top row. Bottom row: the whole trajectories of the probability of hit for the same hitting object as in the top row. (B) Histograms of the probability of hit inferred by models with 32 or 256 LPLC2 units for the four types of synthetic stimuli. (C) The inferred probability of hit as a function of the minimum distance of the object to the fly eye for the miss cases.

Figure 8-Figure supplement 1. The same as (A), but for miss and retreat stimuli.

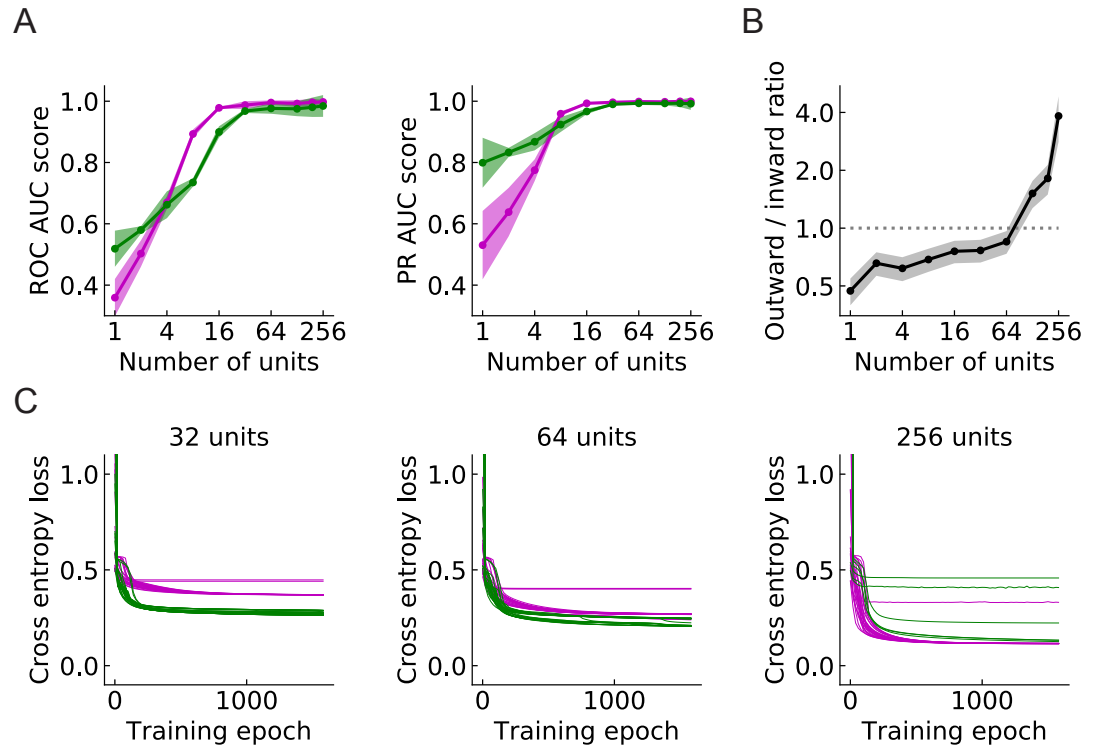


Figure 9. Large populations of LPLC2 units improve performances and favor outward models. (A) Both ROC and PR AUC scores increase as the number of LPLC2 units increases. Lines and dots: average scores; shades: one standard deviation of the scores. Magenta: outward models; green: inward models. (B) The black line and dots show the ratio of the numbers of the two types of the models obtained by varying randomly the initial conditions of the training. The grey shades indicate one standard deviation obtained by assuming the training is a binomial event. The dotted horizontal line indicates the ratio of 1. (C) AS the population of LPLC2 units increase, cross entropy losses of the outward models become lower than the inward models.

Figure 9—Figure supplement 1. Same as in (A) and (B) but for training in different conditions.

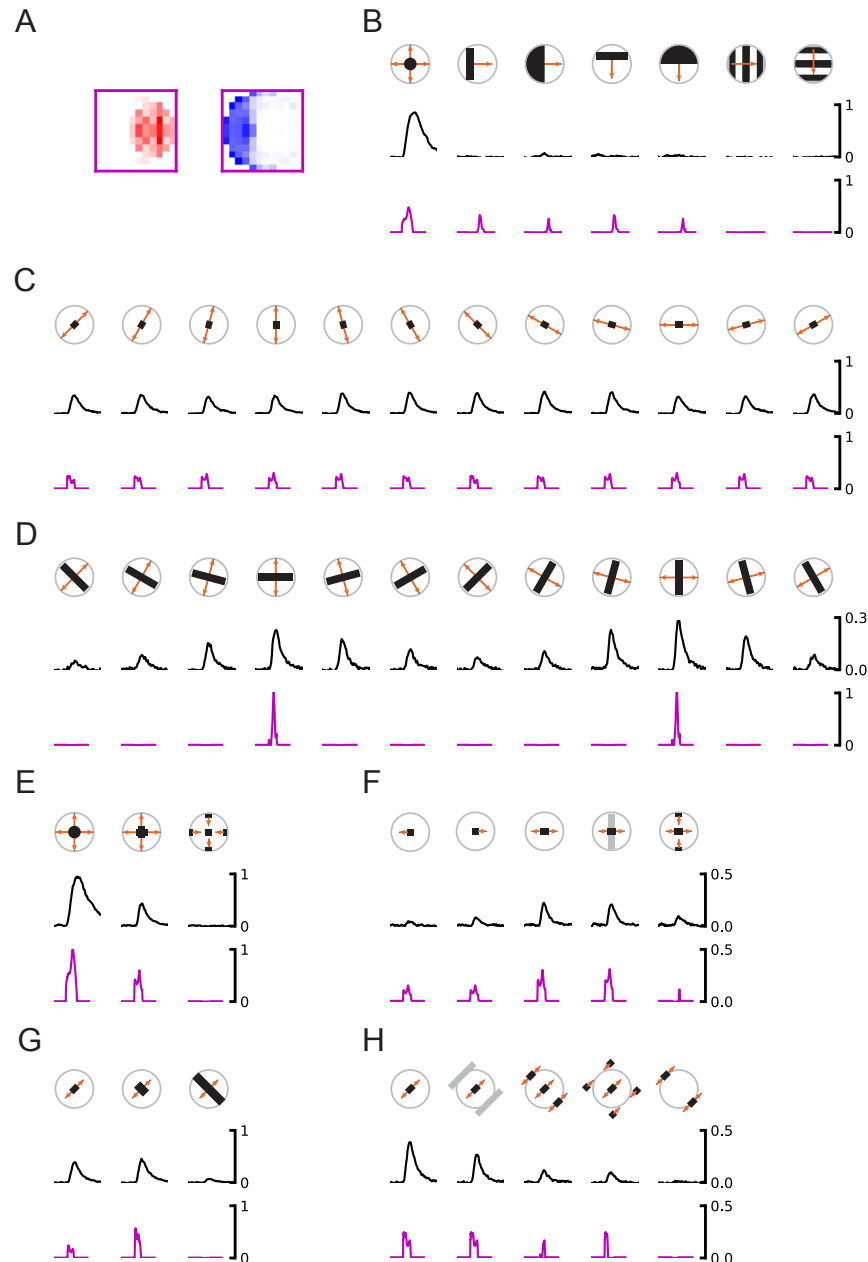


Figure 10. Models trained on binary classification tasks exhibited similar responses to LPLC2 neurons observed in experiments. (A) Excitatory and inhibitory filters of the outward model with 256 units. (B-H) Comparisons of the responses of the model in (A) and LPLC2 neurons. Black lines: data (*Klapoetke et al., 2017*); magenta lines: model. Compared with the ones in the paper (*Klapoetke et al., 2017*), all the stimuli gadgets here except the ones in (B) have been rotated 45 degrees to the frame of reference that is attached to the fly head to match the cardinal directions of the LPLC2 neurons/units.

Figure 10–Figure supplement 1. Same as in the main figure but for a different outward model obtained from the same training procedure.

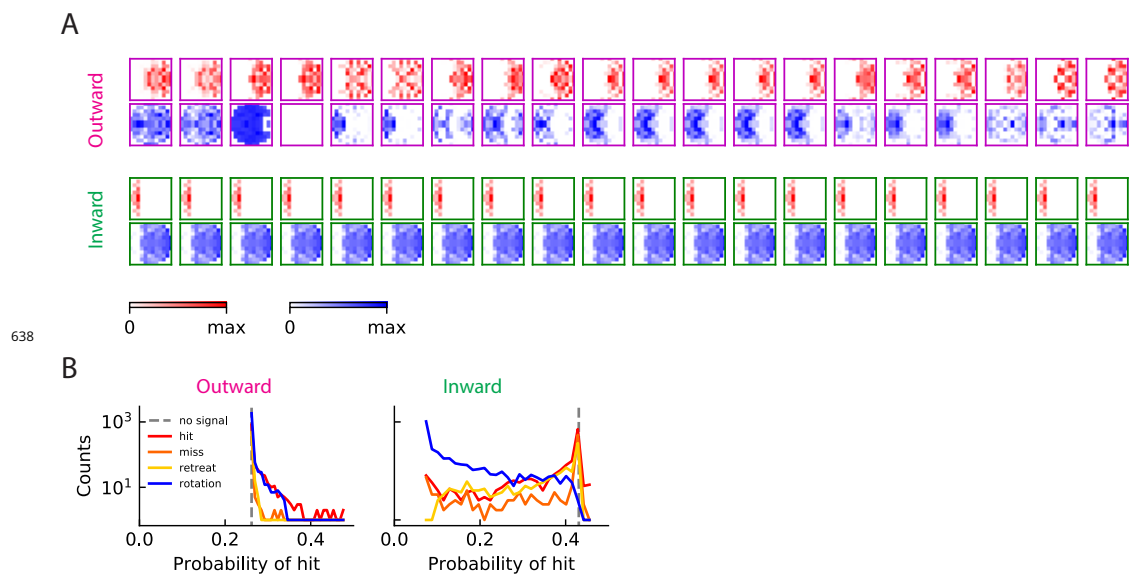


Figure 5-Figure supplement 1. (A) Trained filters: outward model (magenta) and inward model (green). (B) Probability of hit inferred by a single LPLC2 unit for the four types synthetic stimuli.

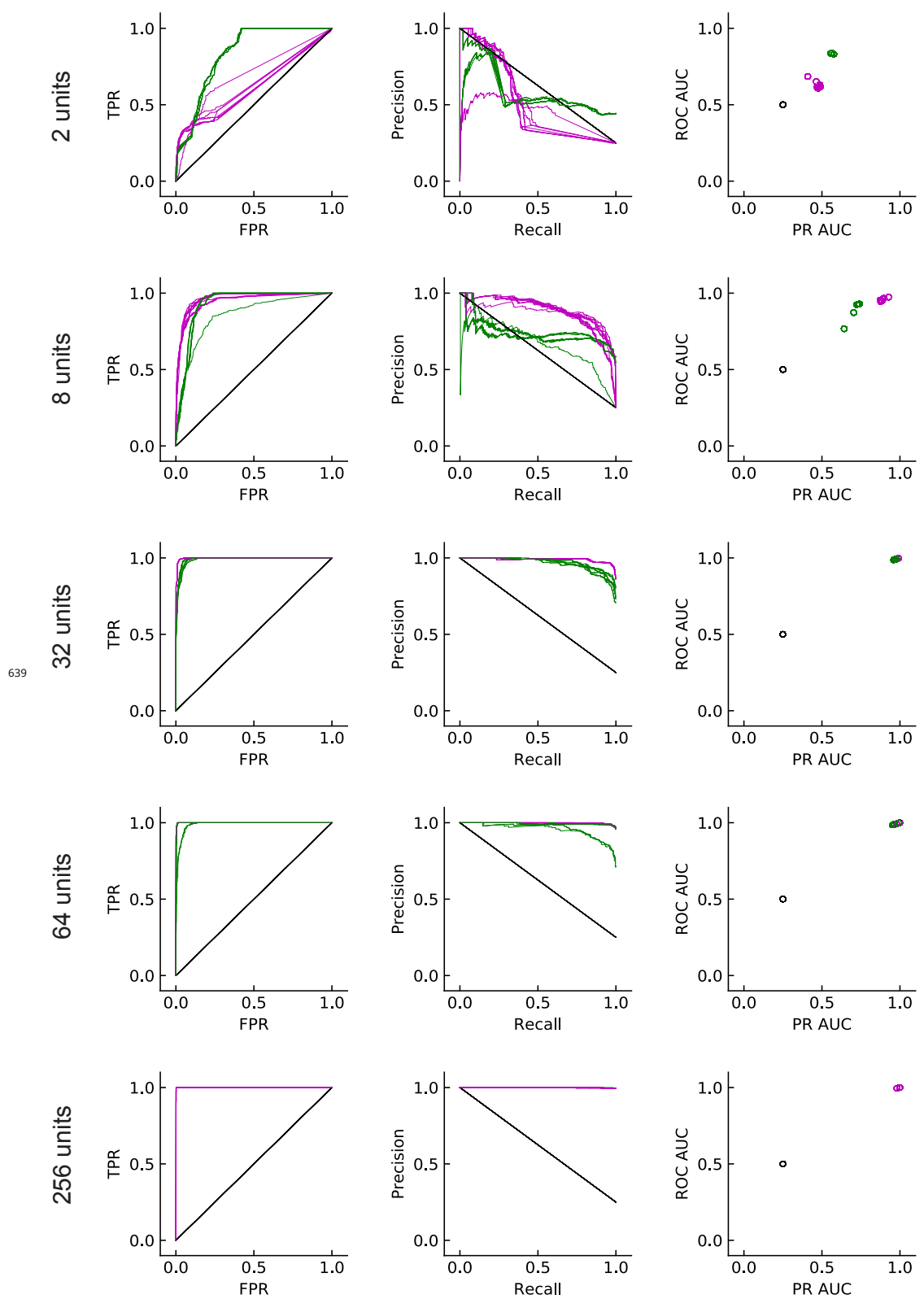


Figure 6–Figure supplement 1. Same as in Fig. 5D) but for models with multiple LPLC2 units.

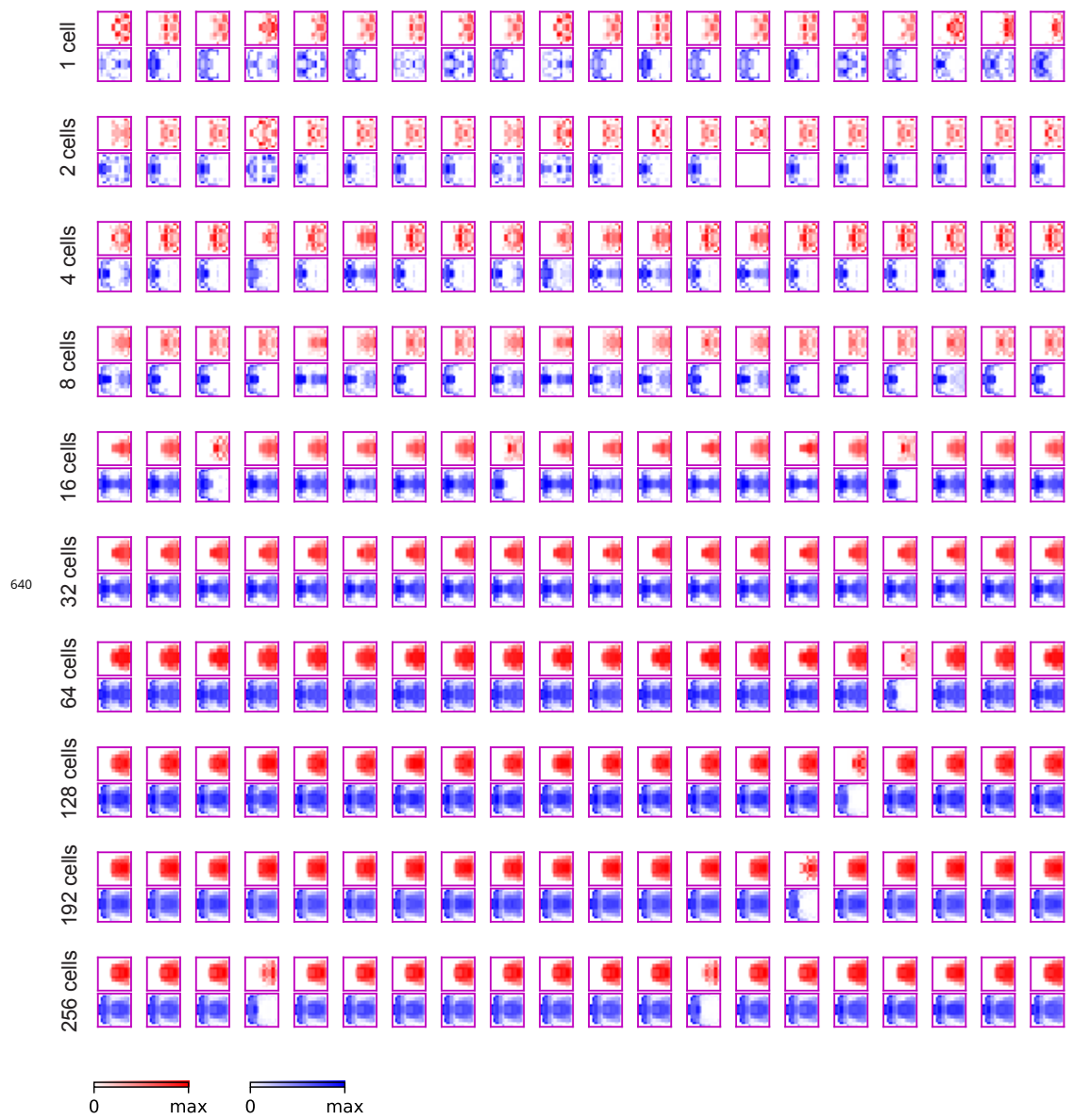


Figure 6–Figure supplement 2.

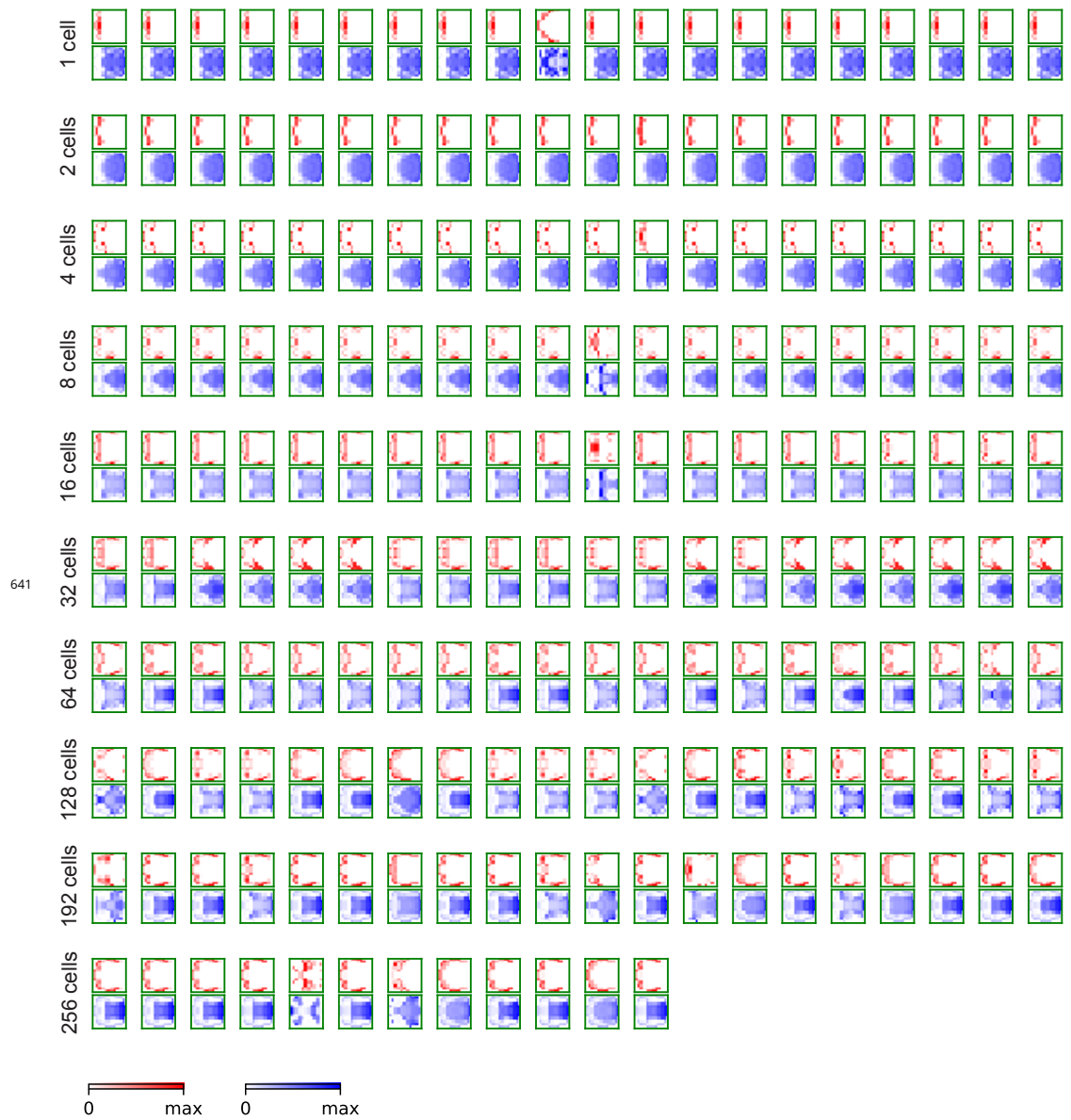
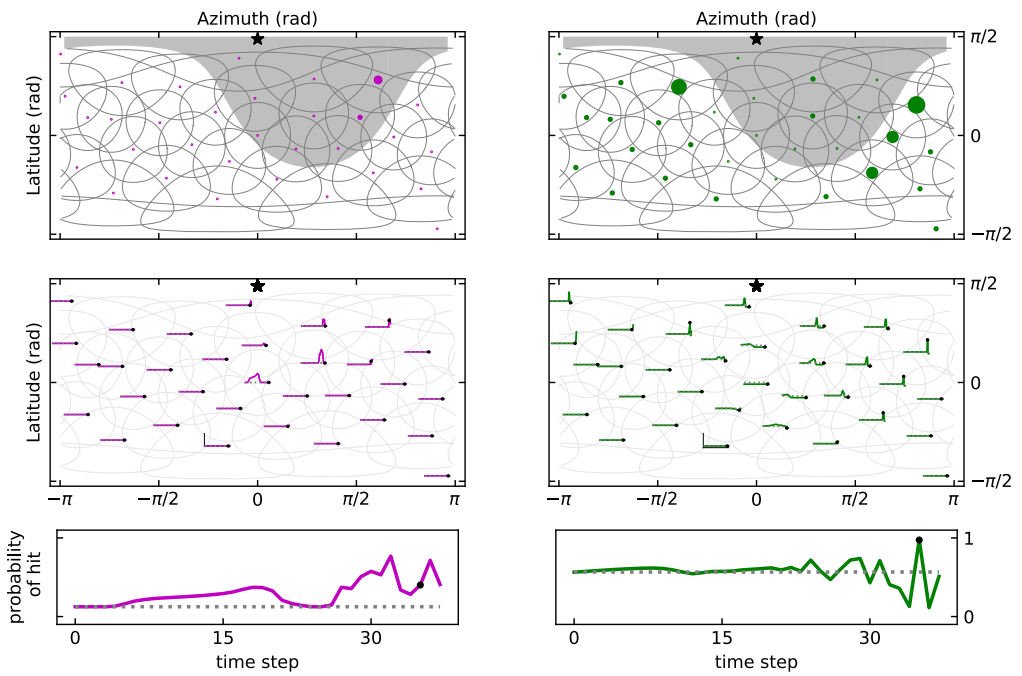
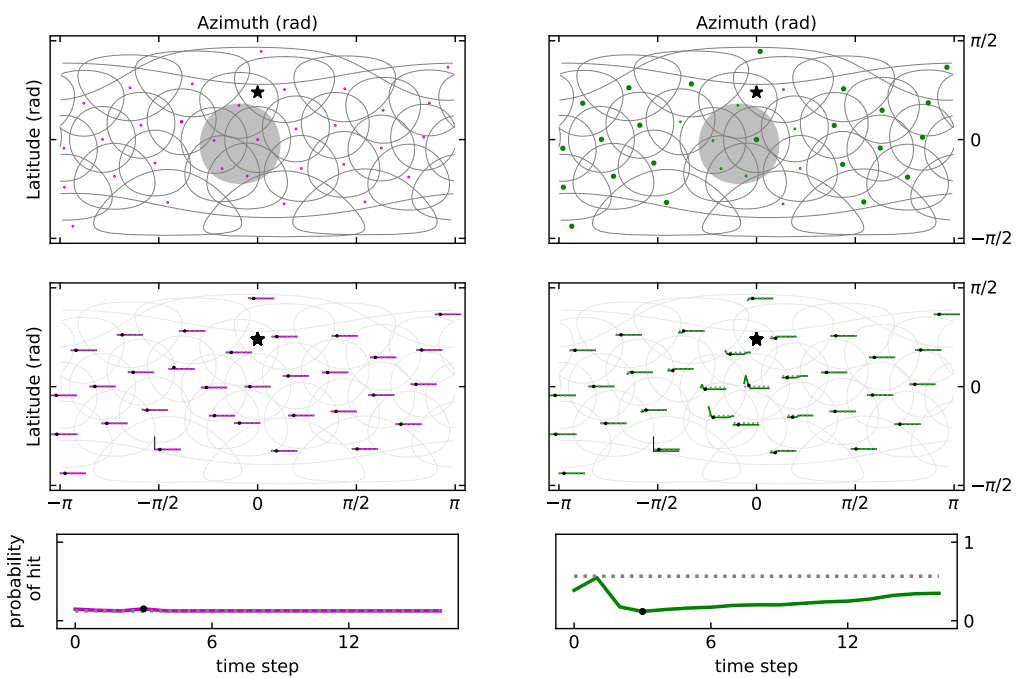


Figure 6–Figure supplement 3.

A

642

B**Figure 8–Figure supplement 1.**

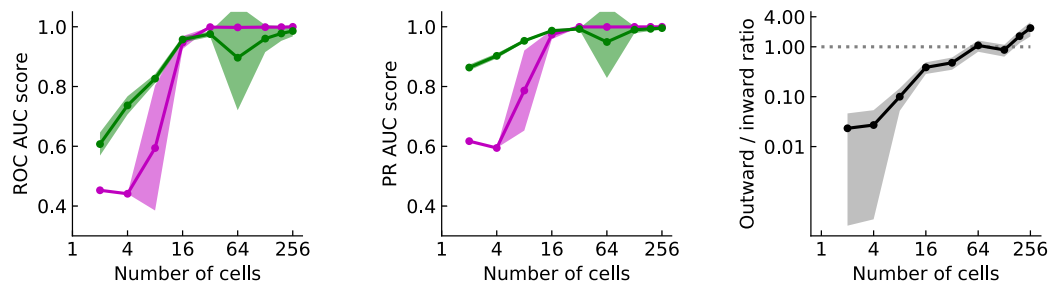
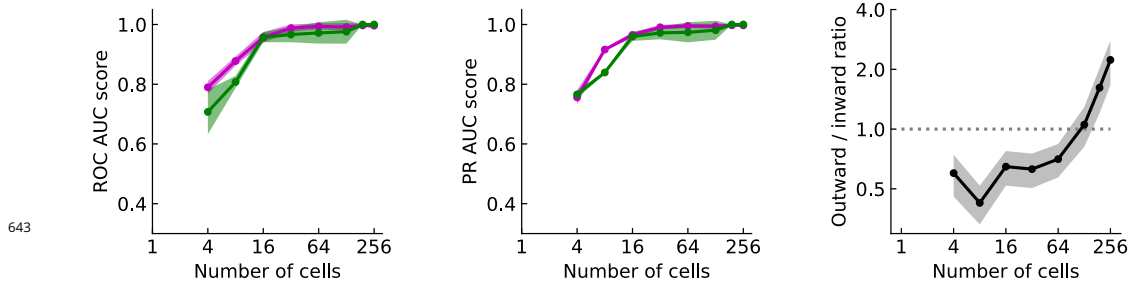
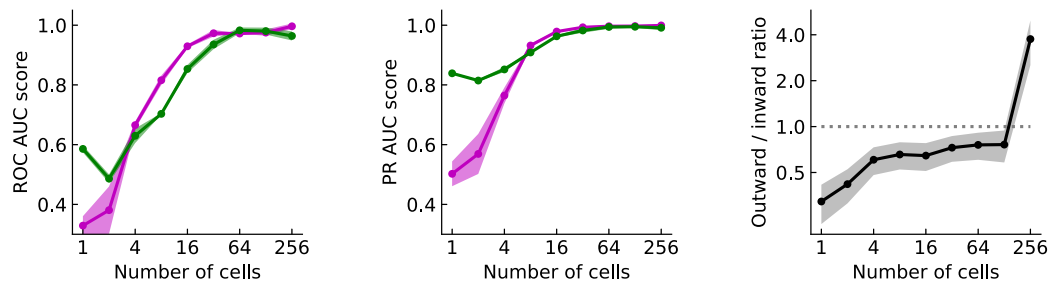
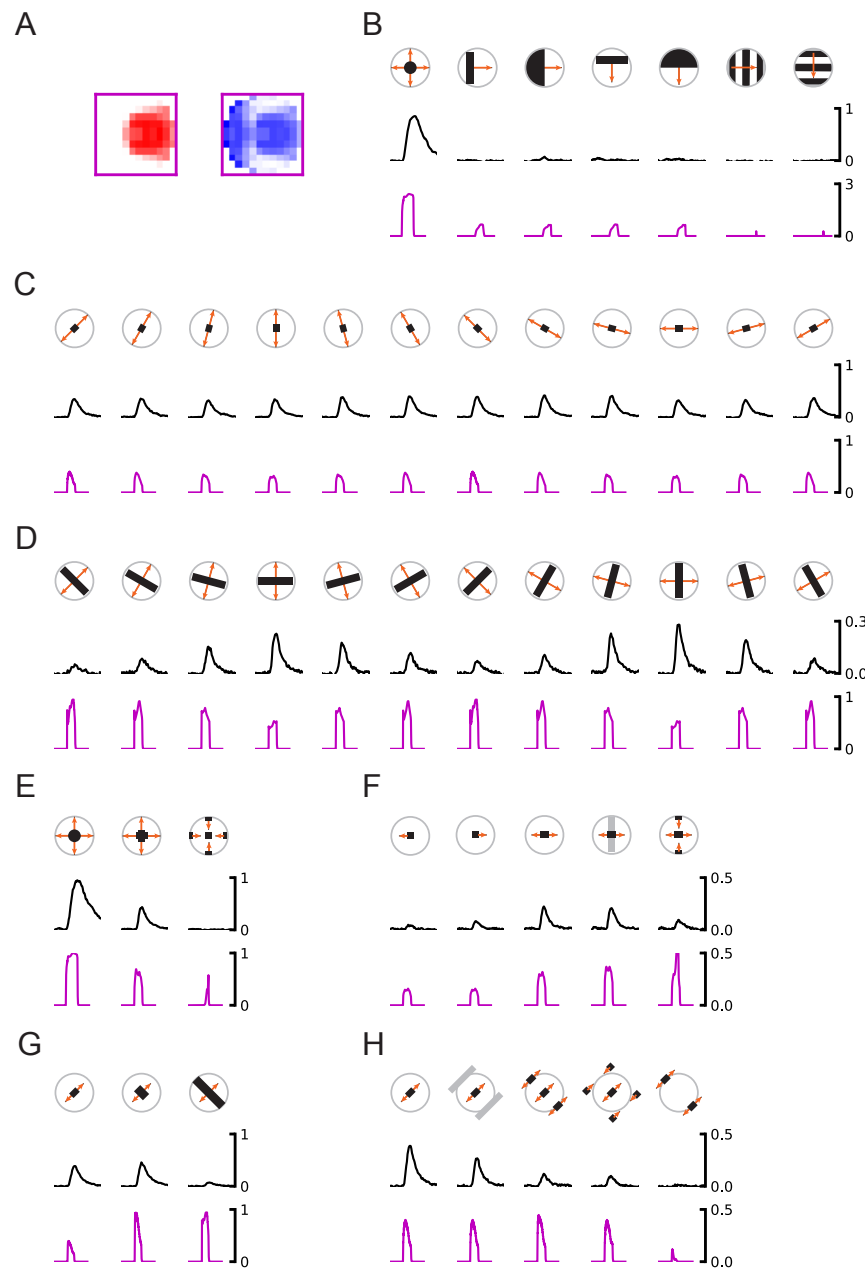
A**B****C**

Figure 9–Figure supplement 1. (A) A different probability model (METHOD). (B) Training without rotation stimuli. (C) Training with larger distances of the objects to the fly eye.

**Figure 10—Figure supplement 1.**